RESPONSE OF PRESTRESSED UHPC PILES SUBJECTED TO FLEXURAL LOADS

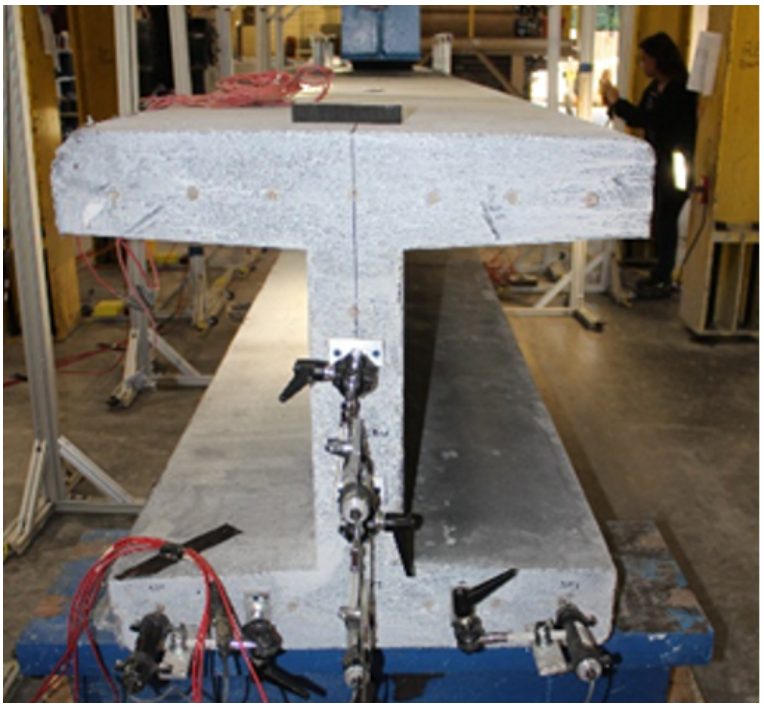

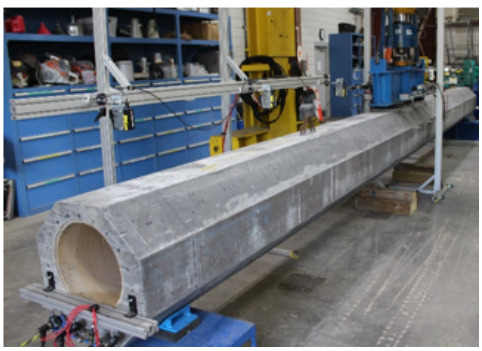

FLORIDA DEPARTMENT OF TRANSPORTATION
M. H. ANSLEY STRUCTURES RESEARCH CENTER

WRITTEN BY:
OLAYIWOLA ADEGBULUGBE, PH.D.
DAVID GARBER, PH.D.
MICHAEL ODELOLA
JAMES DOCKSTADER

REVIEWED BY:
CHRISTINA FREEMAN, P.E.
ARMIN MEHRABI, PH.D., PE., MBA

2025

Acknowledgements

The authors would like to express their sincere gratitude to the many individuals and organizations whose contributions made this research project and report possible.

The development, design, and testing of the ultra-high performance concrete (UHPC) piles documented in this report were made possible through the efforts of numerous collaborators. The 18-inch square and 30-inch H-shaped UHPC piles were designed by the University of Florida, specifically Dr. H.R. Hamilton and Dr. Eduardo Torres, who also developed the test setup and instrumentation plan for those piles. These two pile types were constructed and generously donated by Dura-Stress Inc., with support from Dr. Miles Zemen.

The 24-inch octagonal UHPC pile was developed, built, and donated by Standard Concrete Products. This effort was supported by John S. Lawler (Wiss, Janney, Elstner Associates, Inc.), Maher K. Tadros (e.construct), Mason Lampton (Standard Concrete Products), Elizabeth Nadelman Wagner (Wiss, Janney, Elstner Associates, Inc.), and Adam Sevenker (e.construct) [1].

All testing documented in this report was conducted at the Florida Department of Transportation's (FDOT) M.H. Ansley Structures Research Center. The authors acknowledge and appreciate the critical contributions of the Structures Research Center team, including William Potter, Paul Tighe, Miguel Ramirez, Benjamin Allen, Stephen Eudy, Justin Robertson, and Michael Waters, for their dedication and support in the preparation and testing of the specimens.

The writing and data analysis presented in this report were performed by Dr. Olayiwola Adegbulugbe, Dr. David Garber, Michael Odelola, and James Dockstader. Their efforts in synthesizing the experimental data and documenting the findings are greatly appreciated. Finally, the authors thank Dr. Armin Mehrabi for his careful review of the report.

Disclaimer

Table of Contents

List of Tables

List of Figures

Chapter 1 Introduction

In the pursuit of corrosion-resistant prestressed concrete pile alternatives suitable for extremely aggressive coastal and soil conditions, particularly those characterized by high chloride exposure according to the Florida Department of Transportation (FDOT), this study explores the application of ultra-high-performance concrete (UHPC) materials in piling.

UHPC, a highly versatile material employed in both superstructure and substructure bridge elements, is a high-strength cementitious composite with optimized aggregate proportions, a water-to-cementitious materials ratio between 0.15 and 0.25, and discontinuous internal fiber reinforcement. Comprised of Portland cement, silica fume, fine aggregate, a high-range water-reducing admixture, and fibers, UHPC can be either a proprietary or non-proprietary mixture. It is used in diverse construction applications, including accelerated bridge construction connections, bridge deck overlays, and for seismic purposes.

Renowned for its exceptional durability, mechanical strength, and resistance to environmental aggressors, UHPC achieves heightened durability through a dense matrix characterized by low porosity, low water permeability coefficient, low chloride ion diffusion coefficient, and significantly lower rates of carbonation compared to conventional concrete. These properties result in superior corrosion resistance and an extended service life.

The mechanical attributes of UHPC make it an optimal choice in structures where minimizing material consumption and environmental impact is desirable without compromising structural strength. This leads to the creation of lighter, thinner, and smaller structures. UHPC's mechanical properties, including a minimum compressive strength of 17.5 ksi and a minimum effective cracking tensile strength exceeding 0.75 ksi, enable high bond stress with embedded reinforcement or prestressing strands, resulting in a short development length. The inclusion of fibers enhances UHPC's post-cracking ductility, and the use of UHPC in piles facilitates enhanced drivability with a broader range of hammers and strokes compared to normal or high-performance concrete piles.

The integration of UHPC piles into FDOT projects not only mitigates corrosion concerns but also has the potential to significantly extend the service life of foundation elements, thereby reducing maintenance costs and enhancing the overall resilience of transportation infrastructure.

Through experimental investigations, this report aims to offer an understanding of UHPC pile flexural behavior. The outcome of this research fosters a shift towards advanced materials that align with the evolving needs of FDOT. By elucidating the corrosion-resistant attributes and flexural performance of UHPC piles, this research provides a valuable resource for engineers, policymakers, and stakeholders involved in the planning and execution of durable and sustainable transportation infrastructure projects in the state of Florida.

Chapter 2 Background

In contemporary construction, UHPC has emerged as an advanced material that could transform the design and construction of foundation structures, especially in aggressive coastal and soil conditions. Due to its exceptional strength, durability, and versatility, UHPC is gaining significance in structural applications, but a remaining area of development is the use of piles for buildings, bridges, or other offshore structures.

The attainment of the unique attributes of UHPC lies in its carefully formulated composition in which Portland cement, silica fume, fine aggregate, high-range water-reducing admixture, and fibers are combined. This combination produces a resilient material with optimized properties, making UHPC a viable option capable of being utilized in challenging environmental conditions and high-performance applications.

Research and advancements in UHPC pile technology have sparked investigations into its diverse benefits. This literature review aims to provide an overview of the evolution of UHPC technology, emphasizing its pivotal role in reshaping the landscape of pile construction. By exploring historical development, material composition, flexural behavior, corrosion resistance, design considerations, and practical applications of UHPC piles, the following review aims to contribute to a deeper understanding of the potential advantages and prospects associated with the use of UHPC in piles.

2.1. Historical Development and Evolution of UHPC

The origin of UHPC technology can be traced to the late 20th century, with pioneering experimental efforts to address the limitations of conventional concrete. These efforts were geared towards the following desirable characteristics for an improved concrete material: higher strength, low water permeability, low permeability of chloride ion and other corrosion causing materials, and reduction in the proportion of Portland cement in concrete so that CO_2 emissions during cement production is decreased. The evolution of UHPC marks a transformative journey from conceptualization to widespread utilization in diverse structural applications in several countries across the world.

A pivotal moment in the advancement of UHPC was its initial development, which involved meticulous formulation using a combination of cement, silica fume, quartz flour, fine sand, high-range water reducers, and fibers—commonly steel, synthetic fibers like polypropylene, or high-performance polymer fibers such as carbon fibers. Occasionally, additional additives were incorporated to further enhance its exceptional properties. The optimization of these constituent materials, coupled with progress in production techniques, played a pivotal role in elevating the performance of UHPC.

The structural applications of UHPC have expanded rapidly over time, driven by its numerous advantages over traditional concrete. UHPC's ultra-high compressive strength, typically exceeding 20 ksi [2], allows for the design of slender and lightweight structural elements with reduced cross-sections, resulting in more efficient and aesthetically pleasing designs. Additionally, UHPC's high tensile strength, superior durability, and excellent resistance to corrosion, abrasion, and freeze-thaw cycles make it ideal for use in challenging environments and aggressive exposures. The first recorded structural application of UPHC in North

America was on a pedestrian bridge in Sherbrooke, Quebec, Canada, in 1997 [3] [4]. The present form of UHPC also became commercially available in the United States around year 2000 [4] [5], and its exploration for use in highway infrastructure by the Federal Highway Administration (FHWA) was launched in 2001. It has since then been used in several bridge structures in precast and cast in place applications such as prestressed girders, precast waffle panels for bridge decks, deteriorated bridge deck overlay, retrofit jacket for piles, deck panel joint fills, shear connector pockets, and other connection between prefabricated bridge elements and systems (PBES) [4] [6]. Moreover, its versatility and adaptability to various construction methods, including casting, precasting, and spraying, have further contributed to its widespread acceptance in the construction industry. In addition to meeting project needs or requirements, UHPC can also reduce material consumption, thereby contributing to sustainable construction practices.

To facilitate the understanding and implementation of UHPC products, several agencies in numerous countries have been working on extensive research, standardization efforts, and the development of design guidelines and specifications. Organizations such as the American Concrete Institute (ACI), the Federal Highway Administration (FHWA), and various international standards bodies in Canada, Switzerland, France, Japan, Korea, China, Spain, and others have published guidelines and specifications for the design, production, and testing of UHPC-based structures [7]. As research and development efforts continue, the application of UHPC is expected to further expand, contributing to the advancement of modern construction practices and the development of resilient and durable infrastructure.

2.2. Material Composition and Properties of UHPC

The unique characteristics of UHPC, including its distinctive structure, mechanical properties, and overall performance, set it apart from conventional concrete. Notable features encompass the incorporation of fibers, precise proportions of binder materials, aggregate sizes, and less than 0.25 water-to-cement (W/C) ratio which effectively results in a dense, non-continuous pore structure that effectively minimizes liquid ingress. These specific attributes collectively contribute to a significant enhancement in UHPC's durability when compared to traditional concrete [4] [8].

Steel fibers are commonly integrated into UHPC to bolster its tensile and flexural strength. Serving as reinforcement, these fibers adeptly absorb tensile stresses, thereby reducing cracking and enhancing the material's toughness. Portland cement, supplemented with silica fume or metakaolin, acts as the primary binder in UHPC. These supplementary cementitious materials enhance the density and strength of the concrete matrix through pozzolanic reactions [9]. Quartz flour or silica sand is included as fine aggregates to further densify the matrix and optimize packing density. Furthermore, chemical admixtures, such as superplasticizers and viscosity-modifying agents, are employed to enhance workability, flowability, and curing characteristics. The binder content, minimal void ratio due to the densified matrix, and random steel fiber distribution, contribute to the superior post-cracking stiffness of UHPC compared to conventional concrete mixes. Also, the self-leveling and self-consolidating properties of UHPC enhances ease of placement without the need for mechanical vibration [10].

2.2.1 Proportioning and Mix Design of UHPC

Proprietary UHPC mixtures are typically supplied in three constituents which include preblended dry powder containing the granular constituents (such as cement, silica fume, and fine sand), a separate liquid component that contains a high-range water reducer (HRWR), and the fibers. Alternatively, for custom or nonproprietary UHPC formulations, materials sourced locally can be used. The formulation of UHPC mixtures is deliberately calibrated to ensure an optimal balance between its flowability when mixed and its strength and durability after setting. Customizing the mixture ratios and the process of mixing to accommodate the specific type of mixer being used for production, as well as to align with the unique characteristics of either the proprietary prebagged ingredients or the local materials for custom mixes, is crucial for attaining the desired outcome [11]. Drawing from the experimental findings in literature, the material constituents essential for formulating UHPC are predetermined. Table 1 outlines the recommended median particle size (50th percentile) and the range of particle size distribution (10th and 90th percentiles) for these constituents [12]. Also, based on the findings from previous studies, the recommended mix proportions for designing UHPC are advised in terms of weight ratios as follows [12]:

Cement : Silica fume : Supplemental material = 1 : 0.25 : 0.25

Water : Cement = 0.2 – 0.3

Aggregate : Cement = 1.0 :2.0

Fiber volume fraction = 1.0 % - 2.0 %

Table 1: Recommended material constituents for UHPC matrix design

Material	Particle Size			Notes
	Median	10th percentile	90th percentile	
Water	—	—	—	—
HRWR	—	—	—	For optimal workability and air entrainment
Silica fume	0.2 – 1 µm	0.1 µm	2 µm	Low carbon content
Supplemental material	2 – 5 µm	1 µm	10 µm	Filler effect, spherical shape and pozzolanic reaction preferred
Cement	10 -20 µm	3 µm	40 µm	Low tricalcium aluminate and high combination of tri- and dicalcium silicate
Fine aggregate 1	100 µm	> 50 µm	< 300 µm	High-quality, high-strength, low water absorption, and optimized particle packing
Fine aggregate 2	500 µm	> 300 µm	< 1,000 µm	
Coarse aggregate	—	> 1,000 µm	< 9 µm	

1 inch = 25,400 µm 1 inch = 25.4 mm

Particle packing of aggregates also plays a crucial role in determining the properties of UHPC, especially for achieving a mixture that is both densely packed and workable [11] [12]. Various models have been developed to optimize particle packing in concrete formulations. The Fuller curve employs the concept of

continuous gradation and is characterized by its continuous graded S-shape curve on a single logarithmic graph [13]. Through the work of Fuller and Thompson [13] and Andreasen and Andersen [14], it was proposed that an optimal particle size distribution can lead to minimized porosity and, consequently, enhanced strength. According to authors, P, the percentage of particles passing a sieve with diameter D can be expressed as:

$$P\ (D) = \left(\frac{D}{D_{max}}\right)^{q} \qquad \textbf{Equation 1}$$

Here, D_{max} denotes the largest particle sizes (μm) and q is the distribution modulus, which varies depending on the concrete type. The parameter q ranges from 0 to 1, and a q value greater than 0.50 indicates a coarse mixture, while a value below 0.25 suggests a finer mixture.

The non-applicability of the Fuller curve has been discussed by Brouwers and Radix [15], Willie and Boisvert-Cotulio [12], and Yu et al. [16]. Instead, the modified Andreasen and Andersen packing model was recommended based on its successful use in the optimization algorithms for normal density concrete, light weight concrete and more recently UHPC [12] [16]. The modified Andreasen and Andersen curve shows that optimum particle packing can be achieved when the particle size distribution (PSD) conforms to Equation 2

$$P\ (D) = \frac{D^{q} - D_{min}^{q}}{D_{max}^{q} - D_{min}^{q}} \qquad \textbf{Equation 2}$$

Here, D_{max} denotes the minimum particle sizes (μm)

Ductal® UHPC, a proprietary mixture jointly developed by Lafarge, Bouygues, and Rhodia [17], is commercially available in North America. Ductal mixes offer various material proportions tailored to specific applications, with a typical composition outlined in Table 2. The material proportions were determined, in part, by optimizing the granular mixture, resulting in a finely graded and highly homogeneous concrete matrix. Fine sand, typically ranging between 150 μm and 600 μm, constitutes the largest granular material, followed by cement particles with an average diameter of approximately 15 μm, and crushed quartz with an average diameter of 10 μm. Silica fume, the smallest particle in the mixture, fills the interstitial voids between the cement and crushed quartz particles. Notably, the largest constituent in the mix is steel fibers which provide micro-level reinforcement within the concrete matrix.

Table 2: UHPC Mix proportion by Ductal®

Materials	Amount (lb/yd^3)	Percent by Weight
Portland Cement	1200	28.5
Fine sand	1720	40.8
Silica fume	390	9.3
Ground quartz	355	8.4
Superplasticizer	51.8	1.2
Accelerator	50.5	1.2
Steel Fiber	263	6.2
Water	184	4.4

Aalborg Portland developed Compact Reinforced composite (CRC) in 1986, which consisted of large quantities of steel fibers (2 to 6 percent by volume), large quantities of silica fume, and a water-binder ratio of 0.16 or lower [18]. The mix proportions of CRC are as shown in Table 3.

Table 3:UHPC mix proportions of CRC by weight

Materials	Proportions
Portland Cement	1.0
Fine Sand[1]	0.92
Silica Fume	0.25
Glass Powder	0.25
HRWR	0.0108
Steel Fibers	0.22 to 0.31
Water	0.18 to 0.20

[1] Maximum size of 0.008 inches (0.2 mm)

The average proportions of the UHPC-class material referred to as Cor-Tuf, developed and characterized by Researchers at the U.S. Army Engineer Research and Development Center [19], is summarized in Table 4.

Table 4: UHPC mix proportions of Cor-Tuf by weight

Materials	Proportions
Portland Cement	1.0
Sand	0.967
Silica Flour	0.277
Silica Fume	0.389
HRWR	0.0171
Steel Fiber	0.310
Water	0.208

Rossi et al. [20] at the Laboratoire Central des Ponts et Chaussees (LCPC) in Paris developed a UHPC-class material referred to as $CEMTEC_{multiscale}$. The proportions of this UHPC are presented Table 5. The authors stated that $CEMTEC_{multiscale}$ is stress hardening in tension and has a very high uniaxial tensile strength greater than 2.9 ksi (20 MPa).

Table 5: UHPC mix proportions for $CEMTEC_{multiscale}$

Materials	Quantity (lb/yd^3)
Portland Cement	1770
Sand	866
Silica Fume	451
HRWR	74
Steel Fiber	1446
Water	303

Quillery, a UHPC company in France, developed BSI® UHPC in 1996 [21]. The proportions of BSI are shown in Table 6. The first industrial use of BSI® occurred in 1998, where it was used to produce beams that were constructed as replacements for steel beams in the cooling towers at the Civaux power plant in France. It was also used to construct the world's first UHPC road bridges on the Bourg-les-Valence bypass in France in 2001 [22].

Table 6: UHPC mix design by BSI concrete

Materials	Proportions
Cement	1
Silica Fume	0.26
Fine Aggregate	0.49
Fibers	0.21
Superplasticizer	0.036
Water	0.19

Other available proprietary mixes include Beton Composite Vicat produced by VICAT (BCV®) and Densit® produced by Densit Aps.

Some work by several researchers in developing non-proprietary UHPC mixtures made with locally sourced materials have been documented by Shahrokhinasab and Garber [23].

2.2.2 Mechanical Properties of UHPC

This section provides a summary of some of the mechanical properties of UHPC that make it a promising material.

Design compressive strength: the regression analysis of tested UHPC specimens by Graybeal [17] yielded an equation to estimate UHPC compressive strength as follows:

$$f'_{ct} = f'_c \left[1 - \exp\left(-\left(\frac{t-0.9}{3}\right)^{0.6}\right)\right] \text{ in MPa units} \qquad \textbf{Equation 3}$$

Where, f'_{ct} is the UHPC compressive strength at age t days, f'_c is the UHPC compressive strength at 28 days, and t is the time after casting in days.

According to literature, proprietary UHPC mixes attain final compressive strength greater than 150 MPa (21.75 ksi) [24] [25].

Tensile stress-strain behavior is characterized by four distinct phases, as observed in Figure 1. These phases delineate the response of UHPC to direct tension and encompass key transitions in its mechanical behavior. The initial phase, known as the elastic phase, is characterized by linear-elastic response devoid of crack formation. Subsequently, the emergence of hairline cracks occurs, indicating the initiation of plastic deformation which progresses into the phase marked by the development of multiple closely spaced cracks

within the UHPC matrix. After this comes the crack saturation phase, characterized by strain hardening and the proliferation of larger cracks within the UHPC matrix. Finally, the localization phase signifies the achievement of ultimate tensile strength, culminating in a decline in strength. During this phase, a single crack significantly enlarges, resulting in the pull-out of fibers from the UHPC matrix.

It is imperative to note that the actual tensile behavior of UHPC is influenced by various factors, including the type, content, and distribution of fibers within the matrix. Unlike conventional concrete, UHPC specimens exhibit post-cracking strength attributed to their steel fiber content. UHPC specimens under standard tensile test methods have been shown to demonstrate a first-cracking strength greater than 0.87 ksi (6 MPa) [4].

Also, Graybeal [4] [17] concluded that the tensile strength (f_t) of UHPC can be related to its measured compressive strength (f_c') through the equations below in MPa units:

$$f_t = 7.8\sqrt{f_c'} \text{ or } 8.3\sqrt{f_c'} \text{ (depending on the method used for steam cured specimens)} \qquad \textbf{Equation 4}$$

or

$$f_t = 6.7\sqrt{f_c'} \text{ (for untreated specimens)} \qquad \textbf{Equation 5}$$

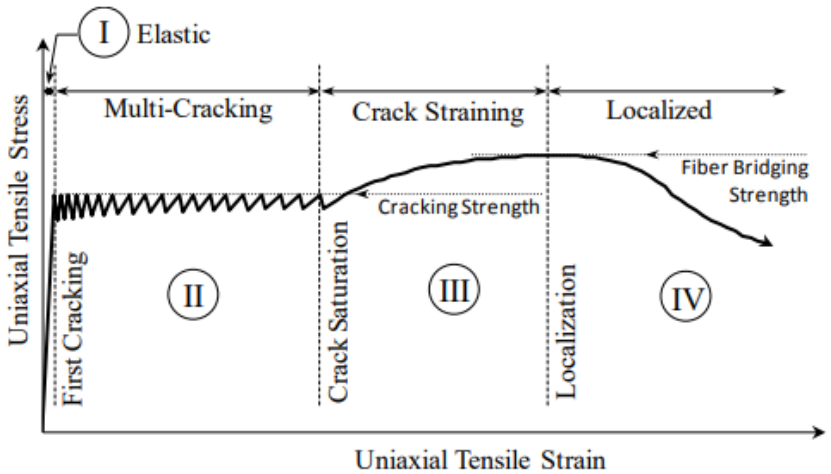

Figure 1: Idealized uniaxial tensile mechanical response of a UHPC [26]

Elastic Modulus: the elastic modulus of UHPC surpasses that of conventional normal strength concrete and is influenced by the final concrete compressive strength. The proposed equation for modulus of elasticity (E_c) in the absence of measured data proposed by AASHTO LRFD guide specifications for structural design with UHPC is shown below. This equation is also referenced by El-Helou and Graybeal [27].

$$E_c = 2,500K_1 f_c'^{0.33} \text{ in ksi units} \qquad \textbf{Equation 6}$$

where, K_1 is the correction factor for modulus of elasticity to be taken as 1.0 unless determined by physical test.

Flexural strength: UHPC exhibits remarkable tensile capacity, well beyond the initiation of initial tensile cracking and retaining this strength until the eventual pullout of the fiber reinforcement. This exceptional ductility distinguishes UHPC from conventional concrete materials. Moreover, in terms of flexural behavior, UHPC displays a more linear load-deformation response in comparison to conventional concrete, particularly leading up to compressive failure. This linear behavior reflects the superior mechanical properties and structural integrity inherent in UHPC, making it an optimal choice for applications demanding high bending resistance and durability. Additionally, UHPC's flexural performance is influenced by its exceptionally high compressive strength, surpassing that of both conventional and high-performance concretes. This superior strength enables UHPC to withstand substantial bending loads without compromising its structural stability or integrity [17]

2.3. UHPC in Precast Piles

Suleiman et al. [28] evaluated the behavior of UHPC piles using large-scale tests and analytical procedures. They drove two 35 ft. long 10 by 10 in. UHPC H-Pile using a DELMAG D19-42 hammer with a 2 in. thick hammer cushion. Due to hard driving conditions, the plywood cushions for the UHPC piles disintegrated, and both piles were effectively driven without a pile cushion for about 2 ft. to 4 ft. Remarkably, neither of the UHPC piles suffered damage during driving. Similarly, Ng et al. [29] conducted drivability analysis on two UHPC H-Piles and determined that the measured maximum stresses of the UHPC piles were well below the allowable driving limits. Furthermore, they concluded that the UHPC test piles exhibited exceptional performance during driving operations.

The findings in these studies suggest that the utilization of UHPC in piles makes them less prone to damage during handling transportation and driving. UHPC piles offer the flexibility of being driven using a broader range of hammers and strokes compared to conventional concrete piles. Additionally, their superior strength, durability and higher load capacity allow for the use of smaller pile cross-sections and/or a reduced number of piles required for a given project. Furthermore, the high durability of UHPC can contribute to low maintenance costs over the life cycle of the pile.

Chapter 3 Experimental Testing Program

3.1. Specimen Description

The research utilized four prestressed UHPC test specimens, each measuring 30 ft with varying cross-sections: an 18-inch square pile, two 30-inch H-Piles, and a 24-inch octagonal pile. These piles were constructed by two different precasters in Florida: Durastress and Standard Precast Products (SCP). Figure 2 illustrates the details of these piles.

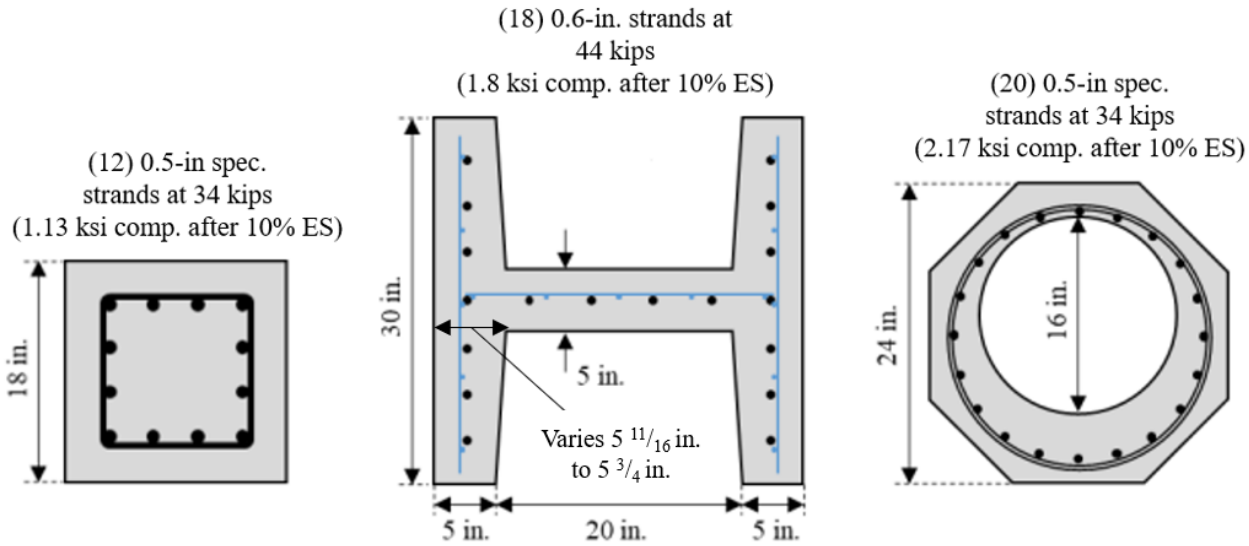

Figure 2: Details for tested UHPC piles: (a) 18-inch square pile cast at Durastress, (b) 30-inch H-piles cast at Durastress, and (c) 24-inch octagonal pile cast at SCP

3.2. Pile Materials and Fabrication

The materials utilized for the construction of test piles primarily comprised UHPC and prestressing strands. The square pile and H-Pile, manufactured on the 10th of January and 20th of June 2019, respectively, at Durastress, were constructed using Cor-Tuf® UHPC. For prestressing, the 18-inch square pile employed twelve 0.5-inch diameter (special) seven-wire 270 ksi low-relaxation steel strands, while the 30-inch H-Piles each employed eighteen 0.6-inch diameter seven-wire 270 ksi low-relaxation steel strands. Although spiral information for the square pile was not provided, it was assumed to follow the spiral pattern for a conventional 18-inch square pile in the FDOT standard plan.

The fabrication process shown in Figure 3 for the 18-inch square pile involved placement of forms, spiral placement, positioning of strands through the headers, sequenced strand jacking to a force of 34 kips, maintenance of strand force with grips, and concrete pouring. The UHPC pour was allowed to self-consolidate, followed by leveling and smoothing for proper finishing. The curing process consisted of simply placing a tarp over the concrete to limit evaporation from the surfaces, and only ambient heating, imparted by the warm Florida climate, was relied upon to cure the UHPC. [1] Once the pile was cast and cured, the strands were symmetrically cut at both ends using the flame cutting technique after which the

pile was removed from the mold. The details of concrete compressive strength measurement taken for the square specimen from day 1 to day 28 is summarized in Table 7. For each batch of concrete mix, labeled A, B, and C, three cylinders were tested on the 28th day, yielding a recorded average strength of 26.65 ksi.

Table 7: Day 1 to 28-day concrete strength for 18-inch square UHPC pile specimen

Age	Measured Strength Batch A (psi)			Measured Strength Batch B (psi)			Measured Strength Batch C (psi)		
1-day	7,282	6,893	—	7,187	7,258	—	6,708	6,139	—
3-day	14,396	15,141	—	14,917	15,436	—	14,330	14,273	—
5-day	19,272	—	—	20,718	—	—	20,718	—	—
7-day	21,336	—	—	20,830	—	—	20,084	—	—
28-day	25,779	26,001	26,248	26,762	27,923	26,129	25,963	26,854	28,142

*Overall average 28-day strength of 26,645 psi

(a) (b)

Figure 3: 18-in. square UHPC pile fabrication showing (a) concrete pouring at one end, and (b) concrete self-consolidating at the other end.

The fabrication process for the 30-inch H-Piles included the placement of external and internal forms, placement of strands and W3.4 mesh, strand jacking to a force of 44 kips, maintenance of strand force with grips, and concrete pouring using the funneling technique depicted in Figure 4. After the concrete cured, the strands were cut, and the forms were removed, as illustrated in Figure 5. With the 28-day concrete compressive strength measurement unavailable for the H-Piles, four cylinders were tested on the day the first of the two H-Pile specimens tested (on 10/2/2019), yielding an average concrete compressive strength of 22.76 ksi as summarized in Table 8.

Table 8: Measured test day concrete strength for the 30-inch UHPC H-Pile specimens

Test Date	Measured Compressive Strength (psi)				Average Compressive Strength (psi)
10/2/19	22,729	22,959	22,313	23,050	22,763

Figure 4: Concrete pouring into the H-Pile forms

Figure 5: H-Pile after removal of forms

During UHPC concrete pouring for the square and H-Piles, balls of unmixed steel fibers were noticed, some of which were removed as shown in Figure 6. It is therefore advised that UHPC precasters look out for and fix such occurrences so that a high level of material uniformity is achieved within a member. Once again,

the curing process consisted of laying a tarp over the concrete to limit evaporation from the surfaces, and only ambient heating was relied upon to cure the UHPC. [1]

Figure 6: Balls of unmixed steel fibers

The fourth specimen, a voided 24-inch octagonal UHPC pile which was cast at SCP, was received at the FDOT Structures Research Center (SRC) on the 9th of March 2018. Concerning the curing process, a tarp was placed over the concrete to prevent evaporation, and outdoor ambient heating was relied upon to cure the UHPC. [30] The materials for fabrication include UHPC concrete, twenty 0.5-inch diameter (special) seven-wire 270 ksi low-relaxation steel strands, steel spirals, and a concrete form tube with an outer diameter of 16 in. Although spiral information for the octagonal pile was not provided, it was assumed to follow the spiral pattern for a conventional solid 24-inch octagonal pile in the FDOT standard plan. While a symmetrical octagonal section was planned prior to casting, the weight of the concrete during pouring caused the interior circular void form to float, resulting in an unsymmetrical cross-section in which the pile was oriented so that the thinner wall thickness was toward the top, as shown in Figure 7. Following this occurrence, the as-built dimensions of the octagonal pile were measured as summarized in Figure 8. Additionally, the average compressive strength measured using two 4 in. by 8in. cylinders, as shown in Figure 9, was 19.21 ksi, as summarized in Table 9.

Figure 7: Voided 24-inch octagonal UHPC pile after removal of forms

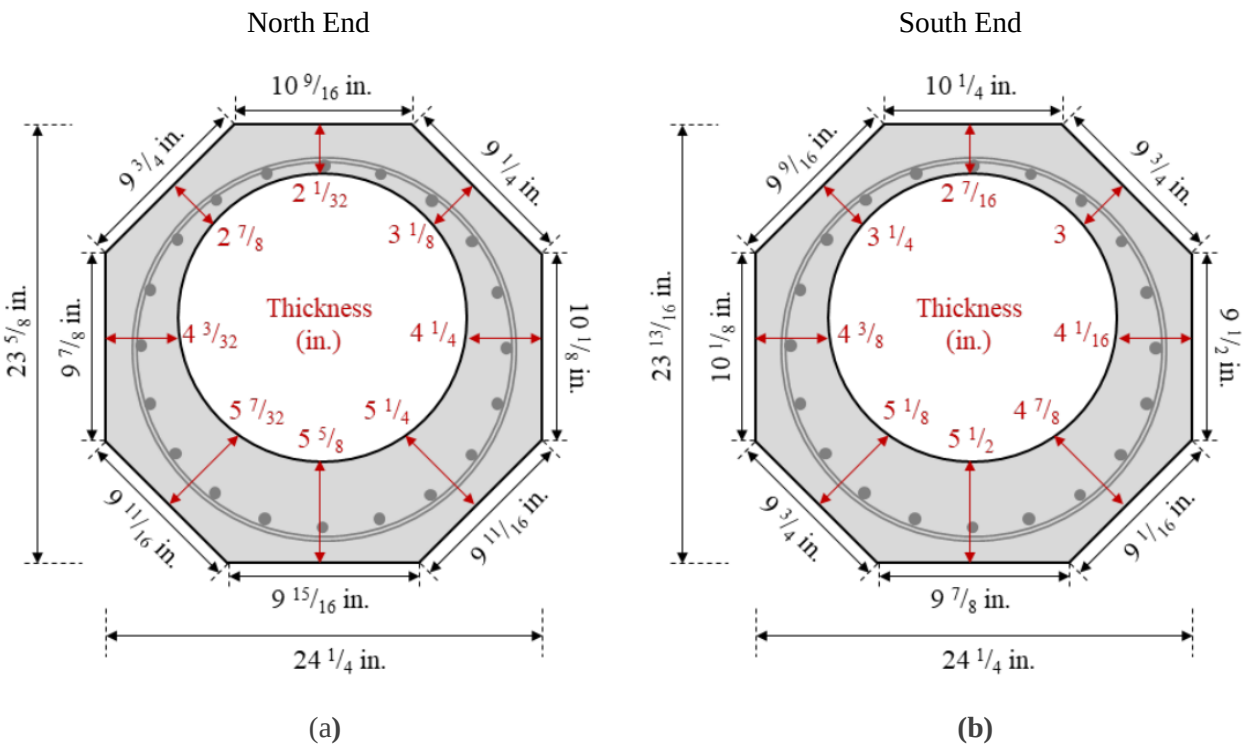

Figure 8: Measured dimensions of 24-inch octagonal UHPC pile at (a) the north end looking south and (b) the south end looking north

Figure 9: Tested concrete cylinders

Table 9: Measured concrete strength for the 24-inch octagonal UHPC pile specimen

Measured Compressive Strength (psi)		Average Compressive Strength (psi)
19,496	18,927	19,212

3.3. Test Setup, Instrumentation and Test Procedure

In this section the test setup, instrumentation, and testing procedure for each of the four UHPC pile specimens are discussed. All specimens were tested in flexure using a four-point loading scheme. Additionally, the 30-inch H-Piles were tested for strong axis flexure and weak axis flexure.

3.3.1 18-inch Square UHPC Pile Specimen

The 18-inch square UHPC pile was tested at the FDOT SRC on April 2, 2019. The loading and support setup for the flexural test of the square pile is as shown in Figure 11. As shown, a W16 x 100 spreader beam was used to transfer load from the actuator to the pile. The spreader beam was placed two thick neoprene bearing pads positioned 4 ft. apart from each other on the face of the pile, this provided a constant moment region between the point loads. The load from the actuator was applied at the center of the spreader beam. The pile was also placed on thick neoprene bearing pads positioned on supports to create a simply supported loading condition with a clear span of 28 ft.

Instrumentation involved strain gauges (SG#), deflection gauges (D#) and slip deflection gauges (SD#) labeled north to south and east to west on the pile. The 60 mm strain gauges used were placed longitudinally to the length of the pile at midspan on the east, west, and top face of the pile, and at 1 ft. to the north and south of the midspan on the top face of the pile as shown in Figure 10. Figure 10 (a) shows an elevation view, and (b) shows a section view. The distances of strain gauges on the sides of the 18-inch square UHPC pile from the top face of the pile are shown in Table 10.

The location of the deflection gauges D1 to D12 and slip deflection gauges SD1 to SD8 is as shown in Figure 12 and Figure 13. Vertical deflection was measured at the supports, load points, midspan, and four additional points along the length of the pile. Note that D4 through D9 were placed on either side of the spreader beam and the SD gauges were installed on the bottom four strands of the pile at the north and south ends of the pile.

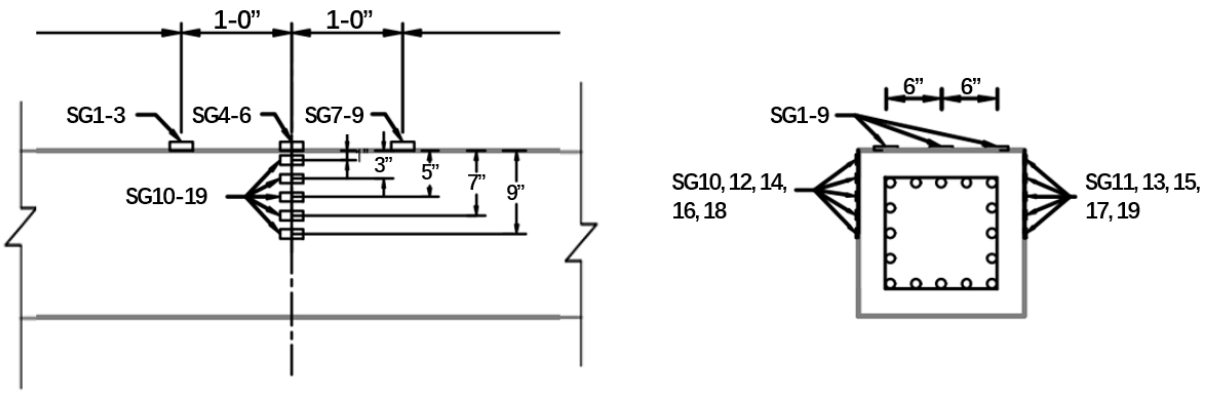

(a) **(b)**

Figure 10: Strain gauge location with respect to midspan - 18-inch square UHPC pile specimen, (a) elevation and (b) cross-section

Table 10: Location of strain gauges on the sides of the 18-inch square UHPC pile

Strain Gauge Label		Distance from Top Face (in.)
East Side	West Side	
SG10	SG11	1
SG12	SG13	3
SG14	SG15	5
SG16	SG17	7
SG18	SG19	9

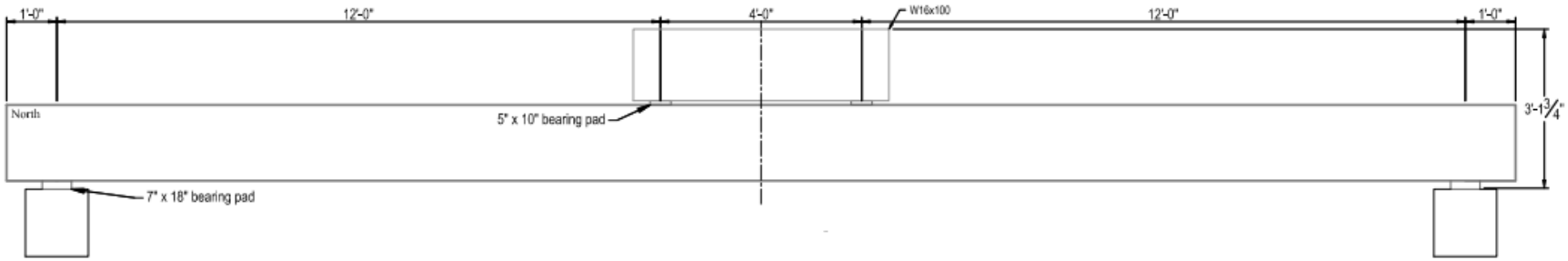

Figure 11: Loading and support setup - 18-inch square UHPC pile specimen

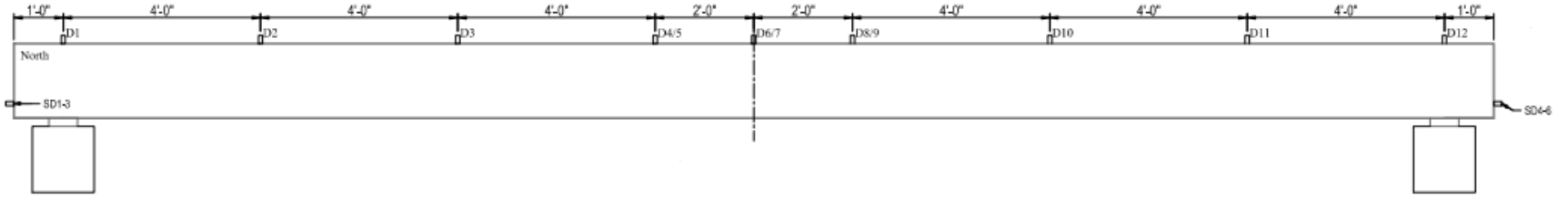

Figure 12: Location of deflection gauges along the length of the 18-inch square UHPC pile specimen

The four-point bending experiment was set up as described in Figure 11 . The gauges were checked to ensure they were in good condition, and malfunctioning gauges were replaced. The load from the actuator was applied at a load rate of 250 lbf/s until the first flexural cracks were noticed. Afterward, the load was held so that crack patterns were observed and mapped. Load application continued with intermittent holds till the specimen failed. Measured data were recorded at a rate of 10 samples per second (10 Hz) through the data acquisition system.

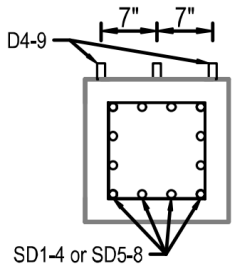

Figure 13: Location of deflection gauges and slip deflection gauges - north/south end view

3.3.2 30-inch UHPC H-Pile Specimen - Strong Axis Flexural Test

A 30-inch UHPC H-Pile was tested for strong axis flexure at the FDOT SRC on October 2, 2019. The loading and support setup for this test is as shown in Figure 14. As shown, a W16 x 100 steel spreader beam was used to transfer load from the actuator to the H-pile. This set up was very similar to that of the square pile flexural test discussed in Section 3.3.1 of this report.

Also, instrumentation involved strain gauges (SG#), deflection gauges (D#) and slip deflection gauges (SD#) labeled north to south and east to west on the pile. The 60 mm strain gauges used were placed longitudinally to the length of the pile at midspan on the east side of the pile, and on the top flange of the H-Pile at distances shown in Figure 15. Note that on the west side of the H-Pile, fiber optic sensors (FOS) were used as shown in Figure 16. The location of strain gauges on the east side of the H-Pile with respect to the top flange is summarized in Table 11. The location of the deflection gauges D1 to D12 and slip deflection gauges SD1 to SD8 is as shown in Figure 17 and Figure 18.

Following gauge installation and necessary checks, load from the actuator was applied at a load rate of 250 lbf/s until the first flexural cracks were noticed. Afterward, the load was held so that crack patterns were observed and mapped. Load application continued with intermittent holds till the specimen failed. Measured data were recorded at a rate of 10 samples per second (10 Hz) through the data acquisition system.

Table 11: Location of strain gauges on the east side of the 30-inch UHPC H-Pile (strong axis test)

Strain Gauge Label	Distance from of Top Flange (East Side) (in.)
SG10	6.75
SG11	9.75
SG12	12.75
SG13	15.75
SG14	18.75
SG15	21.75

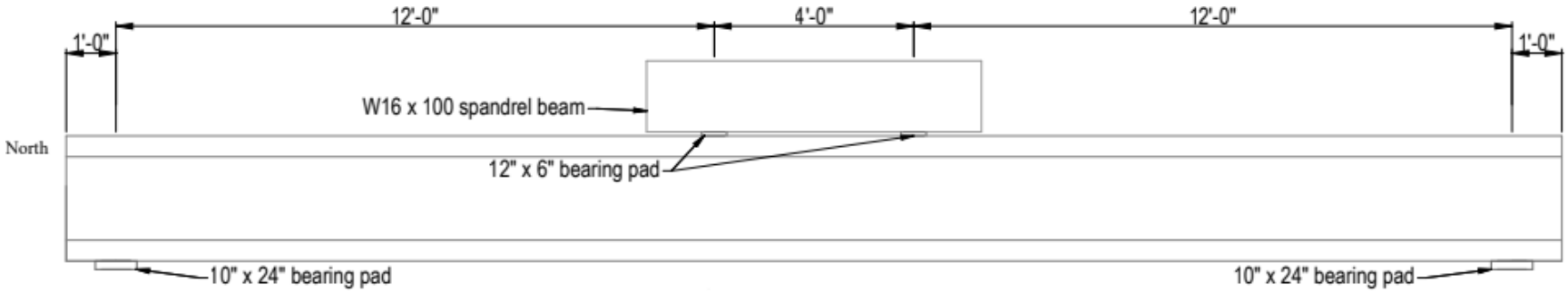

Figure 14: Loading and support setup - 30-inch UHPC H-Pile specimen (strong axis test)

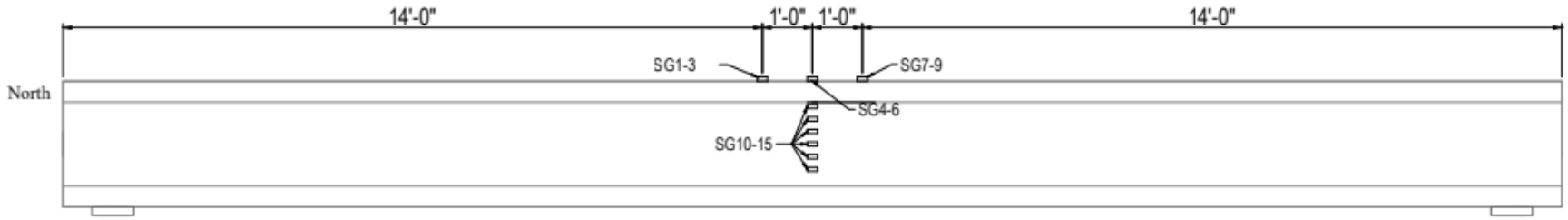

Figure 15: Strain gauge location – east elevation of UHPC H-Pile specimen (strong axis test)

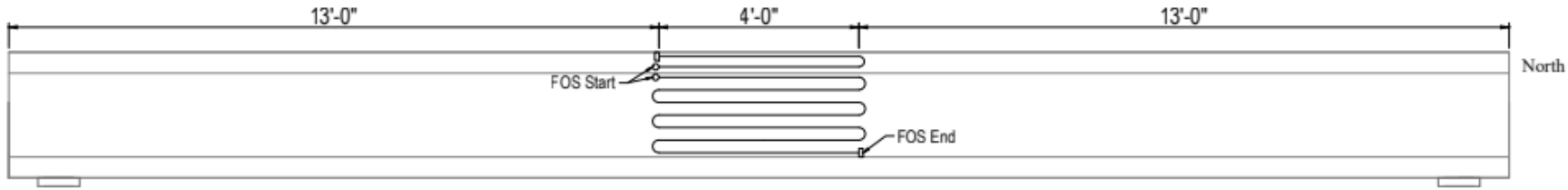

Figure 16: Fiber optic sensor location – west elevation of UHPC H-Pile specimen (strong axis test)

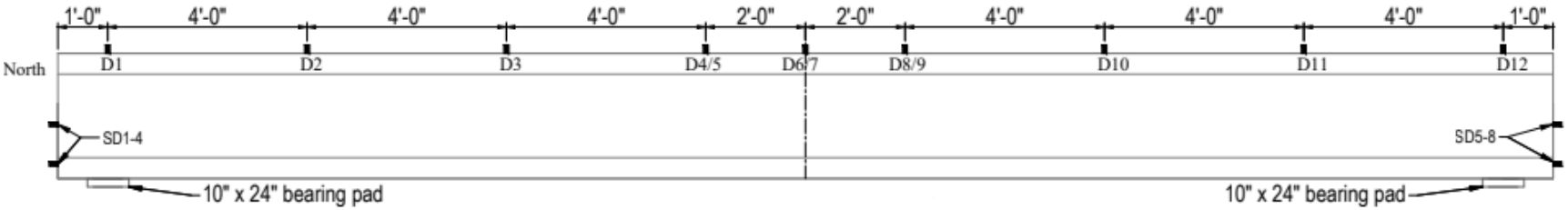

Figure 17: Location of deflection gauges along the length of the 30-inch UHPC H-Pile specimen (strong axis test)

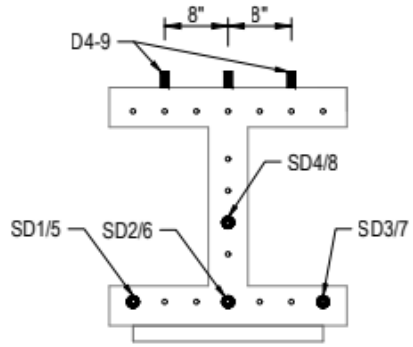

Figure 18: Location of deflection gauges and slip deflection gauges - north/south end vie

3.3.3 30-inch UHPC H-Pile Specimen - Weak Axis Test

Another 30-inch UHPC H-Pile was tested for weak axis flexure at the FDOT SRC on October 9, 2019. The loading and support setup for this test is as shown in Figure 19 and Figure 21. As shown, load was transferred from the 800-kip actuator, first to a W14 x 109 steel spreader beam perpendicular to the H-Pile, then to two C12 x 30 steel double-channel beams positioned parallel to the flanges of the H-Pile. Each C12 x 30 double-channel beam was placed on two thick neoprene bearing pads positioned 4 ft. apart from each other on the flanges of the H-Pile. The H-Pile in-turn was positioned on grout pads placed thick neoprene bearing pads positioned on supports to create a simply supported loading condition with a clear span of 28 ft.

Instrumentation for the weak axis flexure test of the H-Pile involved strain gauges (SG#), deflection gauges (D#) and slip deflection gauges (SD#) labeled north to south and east to west on the pile. The 60 mm strain gauges shown in Figure 22 (a) and (b) were placed longitudinally to the length of the pile at midspan on the east, west, top, and bottom faces of the pile flanges distances shown in Table 12. The location of the deflection gauges D1 to D8 is as shown in Figure 20. Slip deflection gauge locations at the north end of the pile are also shown in Figure 23. This arrangement is replicated on the south end with SD5 to SD8.

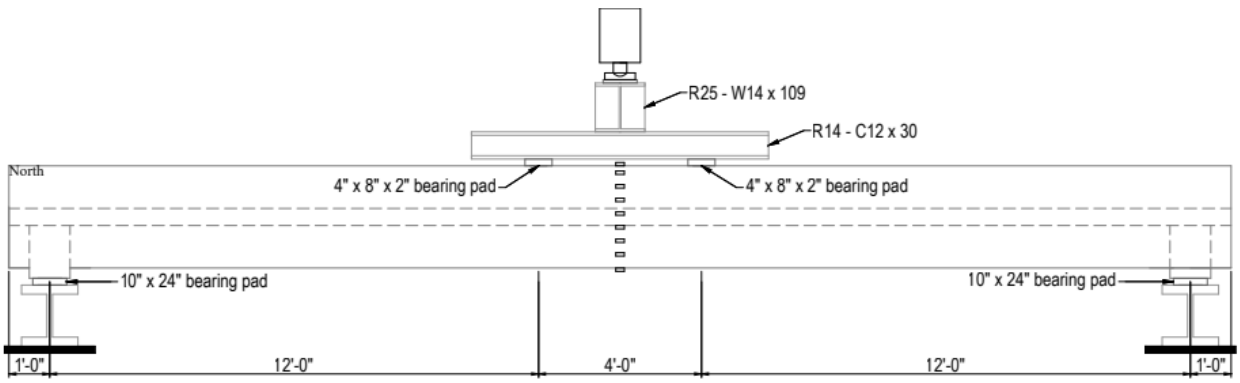

Figure 19: Test setup elevation for H-Pile weak axis test

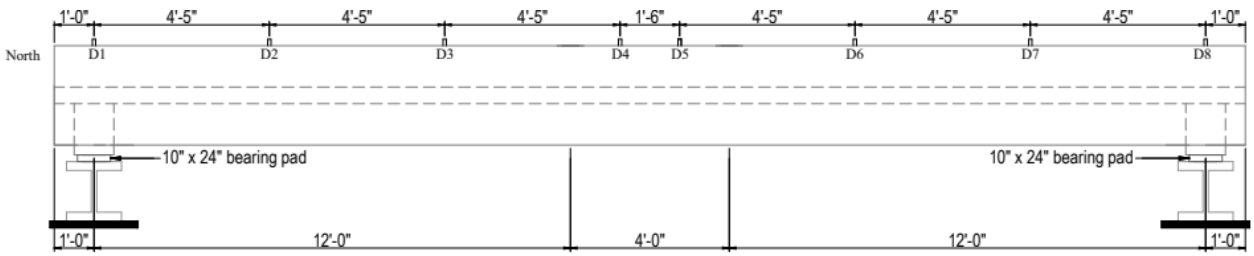

Figure 20: Deflection gauges along pile length for H-Pile weak axis test

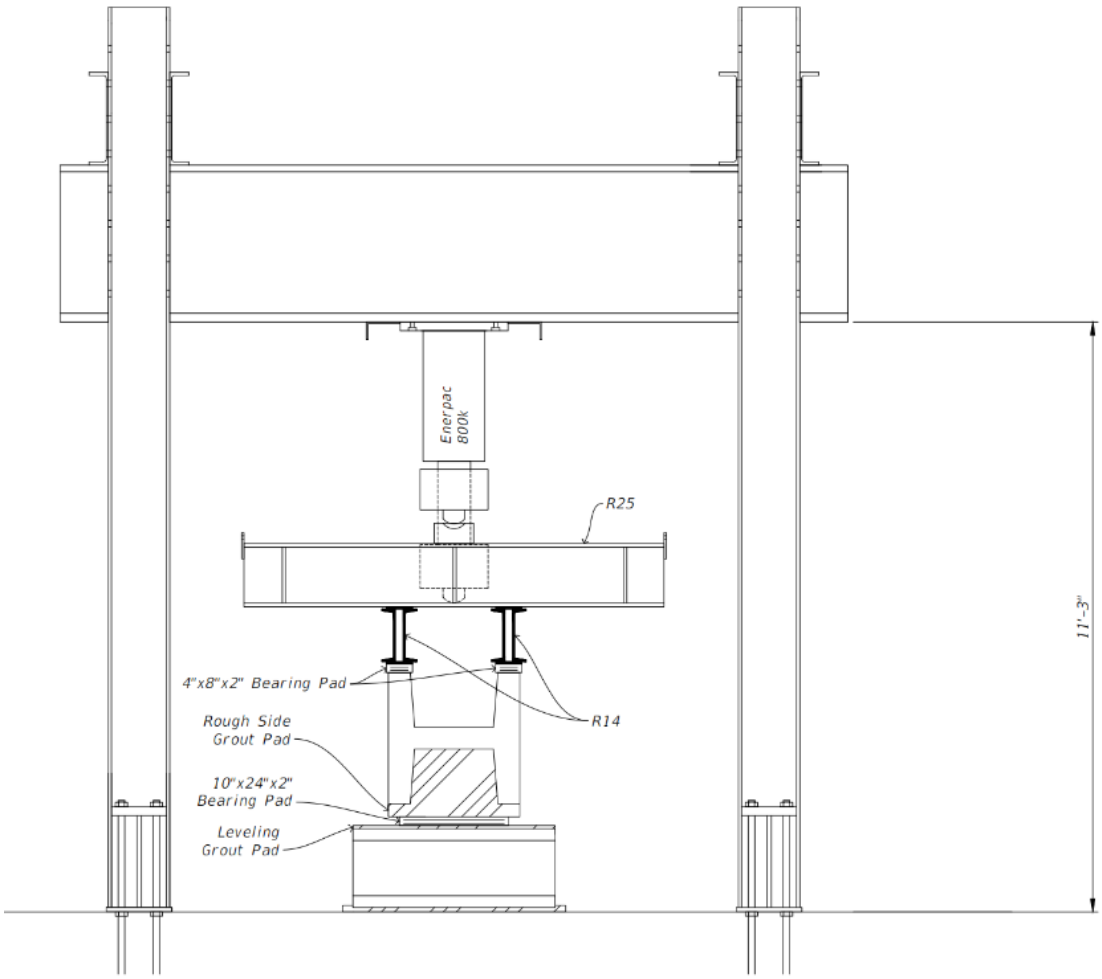

Figure 21: Test setup north end looking south for H-Pile weak axis test

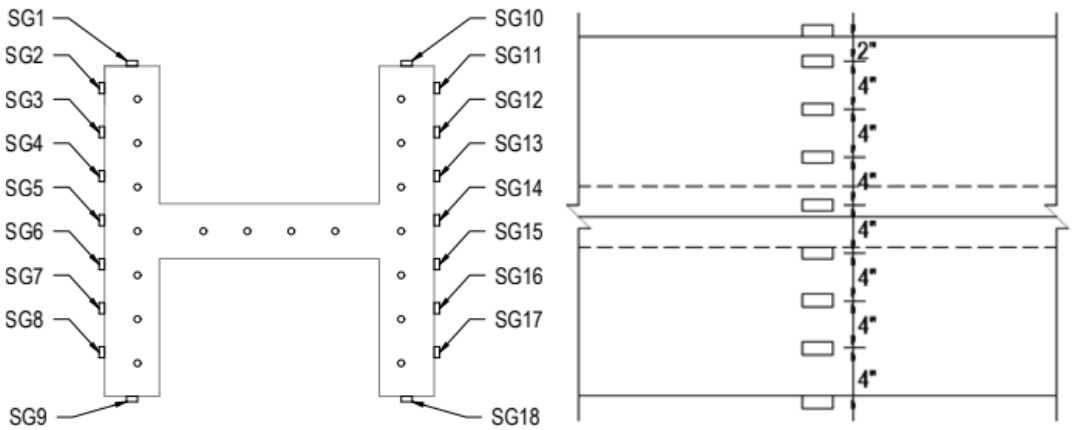

(a) **(b)**

Figure 22: Midspan cross-section showing strain gauge numbering and strain gauge location at midspan for H-Pile weak axis test, (a) cross-section and (b) elevation

Table 12: Location of strain gauges on the sides of the H-Pile (weak axis test)

Strain Gauge Label		Distance from Top Face (in.)
East Side	West Side	
SG1	SG10	0 (top)
SG2	SG11	2
SG3	SG12	6
SG4	SG13	10
SG5	SG14	14
SG6	SG15	18
SG7	SG16	22
SG8	SG17	26
SG9	SG18	30 (bottom)

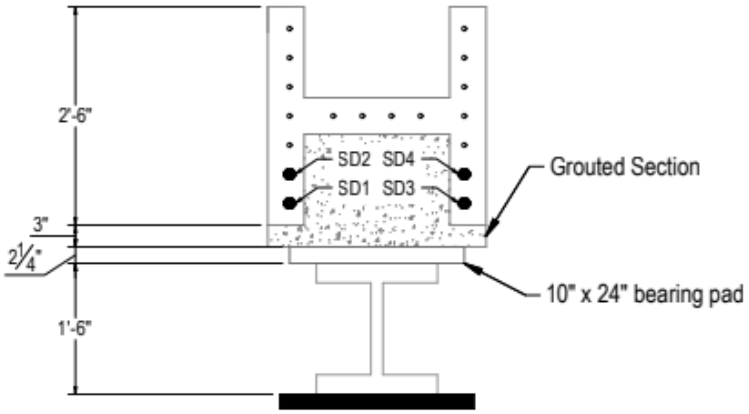

Figure 23: Location of slip gauges at the north end of the H-Pile (weak axis test)

3.3.4 24-inch Octagonal UHPC Pile Specimen Flexural Test

The 24-inch octagonal UHPC pile was tested at the FDOT SRC on April 05, 2018. The four-point loading, and support setup is as shown in Figure 24. Instrumentation involved strain gauges (SG#), deflection gauges (D#) and slip deflection gauges (SD#) labeled north to south on the pile. The 60 mm strain gauges and deflection gauges used were position of the top face of the pile as illustrated in Figure 25 and Figure 26. deflection gauges were installed on the bottom three strands on each end of the pile as depicted in Figure 27.

The loading procedure for this specimen includes application of actuator load at a load rate of 250 lbf/s until the first flexural cracks were noticed, crack pattern mapping at cracking load, subsequent load application with intermittent holds till the specimen failed. Measured data were recorded at a rate of 10 samples per second (10 Hz) through the data acquisition system.

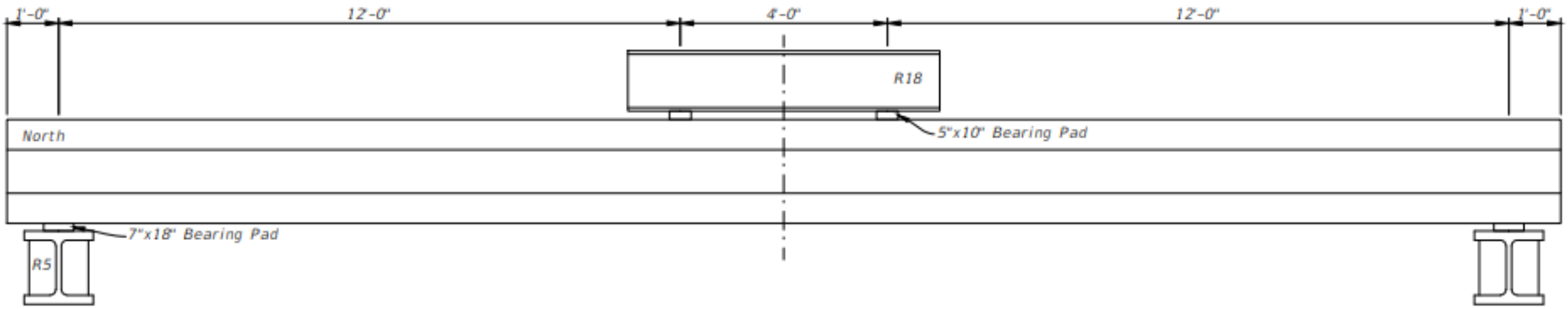

Figure 24: Loading and support setup - 24-inch octagonal UHPC pile specimen

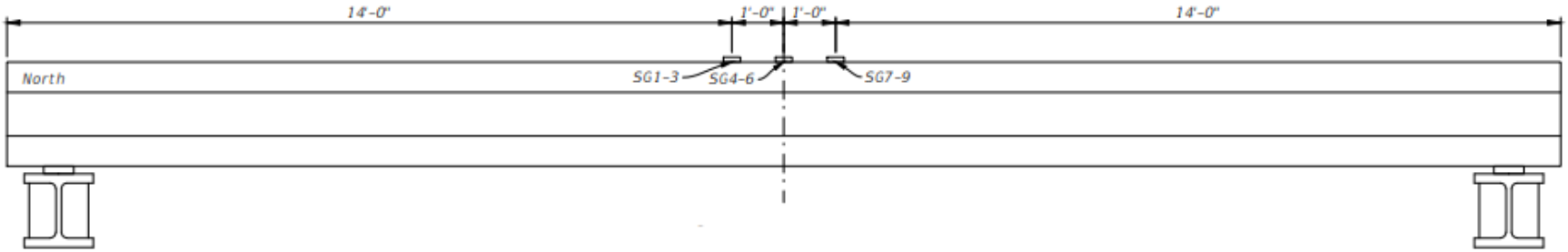

Figure 25: Strain gauge location - 24-inch octagonal UHPC pile specimen

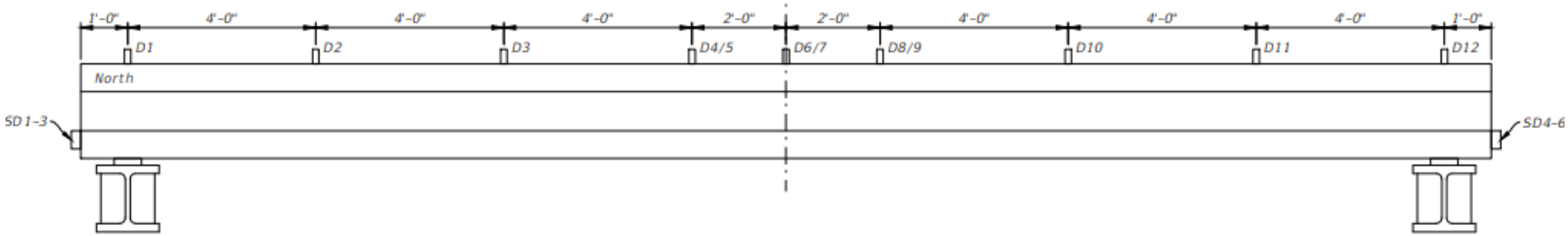

Figure 26: Deflection gauge location - 24-inch octagonal UHPC pile specimen

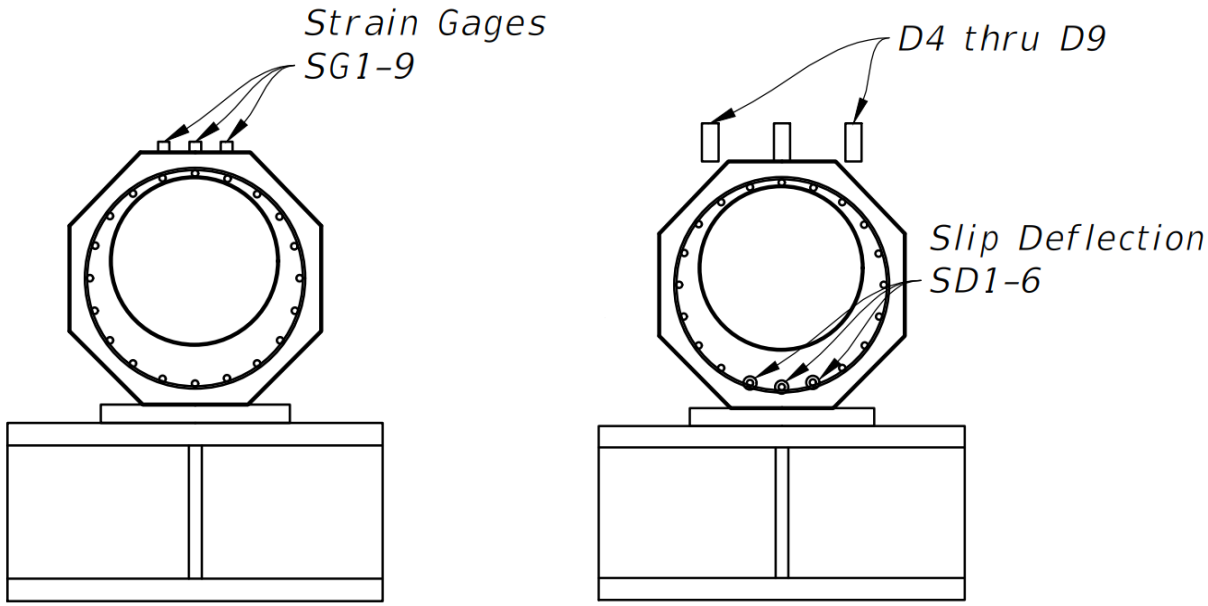

(a) **(b)**

Figure 27: 24-inch octagonal UHPC pile specimen cross-section showing (a) strain, and (b) deflection and slip deflection gauges location

Chapter 4 Flexural Test Results and Observations

In this chapter the results of the four flexural tests conducted on the pile specimens are discussed. A summary of the pile shapes, section properties, strand details, and measured concrete compressive strength of the specimens is provided in Table 13.

Also, the summary of the estimated precompression stress and strain provided in the pile immediately after strand release (assuming 7% elastic shortening (ES) prestress loss) and at the time of testing (assuming 15% total prestress loss (LT)) are shown in Table 14.

Table 13: Summary of UHPC piles tested by FDOT Structures Research Center

Pile Shape	Strand Details	Height, h	Jacking Force, $P_{j,tot}$	Gross Area, A_g	Compressive Strength, f'c	Elastic Modulus, E_c
		(in.)	(kips)	($in.^2$)	(ksi)	(ksi)
Square	(12) 0.5-in.(sp) at 34 kips	18	408	324.0	26.65	7386
H	(18) 0.6-in. at 44 kips	30	792	412.5	22.76	7012
Octagonal	(20) 0.5-in.(sp) at 34 kips	24	680	281.8	19.21	6630

Table 14: Summary of estimated precompression due to prestress

Pile Shape	Estimates after Strand Release (7% ES)		Estimates after Assumed Total Losses (15% LT)	
	Stress (ksi)	Strain (με)	Stress (ksi)	Strain (με)
Square	1.17	159	1.07	145
H	1.79	255	1.63	233
Octagonal	2.24	339	2.05	309

4.1. Flexural Test Results

4.1.1 18-inch Square UHPC Pile Specimen

The measured load versus deflection plots at different points along the length of the pile are shown in Figure 28. These plots have the support settlement removed from the deflection. The deflection at the load points and midspan are shown as the average of the two vertical displacements measured toward the east and west faces of the member. A non-linear response of the member began around 32 kips (equivalent to a 226 k-ft. moment), which is assumed to be the approximate cracking load. The ultimate load was measured as 83.76 kips (equivalent to a 537 k-ft. moment). Figure 29 shows a plot of deflection along the length of the pile at different applied loads. As shown the pile reached a deflection of 4.05 in. at the ultimate load, however, the

pile continued to sustain load till complete failure occurred at about 71.71 kips. The corresponding maximum deflection at the failure load was 4.56 in.

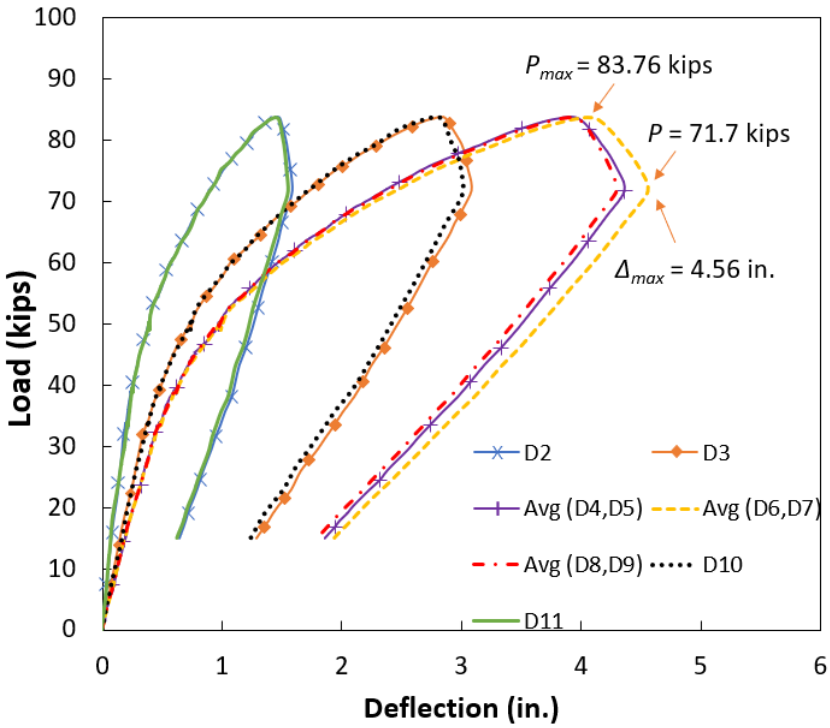

Figure 28: Load versus deflection for 18-inch square UHPC pile

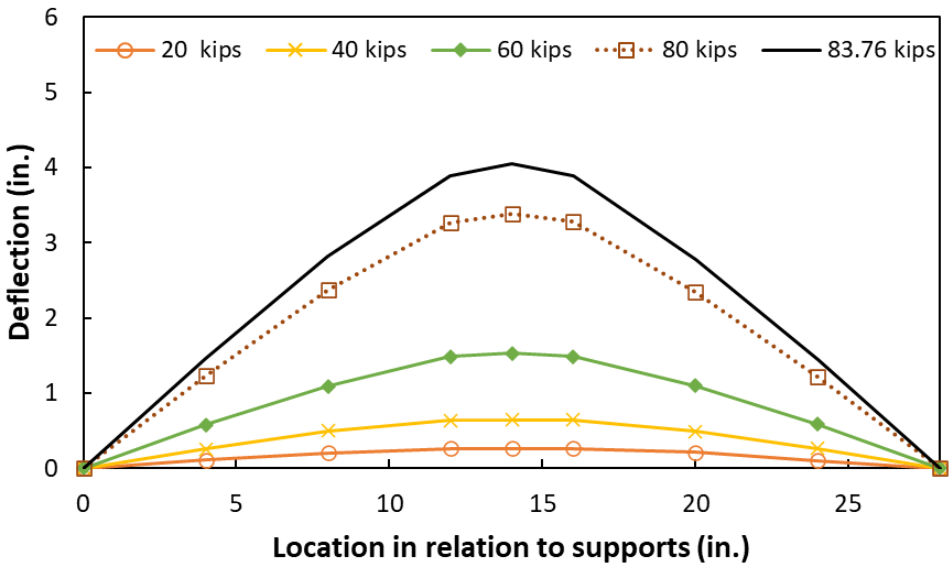

Figure 29: Deflection versus distance from north support for 18-inch square UHPC pile

The moment in the pile when load is applied is a combination of the moment from the applied load and the self-weight moment. The moment at the cracking load and maximum load can be found as shown in the following calculations where ρ_c is the UHPC density, A_g is the gross cross-sectional area of the pile, a is

the distance between a support and a load point, P is the applied load, P_{cr} is the cracking load and P_{max} is the maximum load applied.

Approximate self-weight, $w_{sw} = \rho_c A_g = (0.155\ kcf)(324\ in.^2)\left(\frac{1\ ft.}{12\ in.}\right)^2 = 0.349\ {}^{k}/_{ft.}$

Self-weight moment at midspan, $M_{sw,max} = \frac{w_{sw}L^2}{8} = \frac{({}^{0.349k}/_{ft.})(28\ ft.)^2}{8} = 34.2\ k-ft.$

Moment at midspan (ignoring weight of spreader beam) due to load P, $M_{mid} = 0.5Pa$

Cracking moment, $M_{cr} = 0.5P_{cr}a + \frac{w_{sw}L^2}{8} = 0.5(32\ kips)(12\ ft.) + 34.2\ k-ft. = 226\ k-ft.$

Maximum moment at failure, $M_{max} = 0.5(83.76\ kips)(12\ ft.) + 34.2\ k-ft. = 537\ k-ft.$

Maximum moment at crushing load, $M_{71.1\,k} = 0.5(71.7\ kips)(12\ ft.) + 34.2\ k-ft. = 464\ k-ft.$

The concrete strain gauges installed on the pile as described in Section 3.3.1 were attached after the initial precompression from the prestressing strands occurred. The strain from the precompression can be estimated as shown below. This precompression strain was determined with the assumption that there were only axial strains from the precompression because of the symmetrical strand pattern in the pile and that the total prestress loss was 15 %.

Estimated precompression force (after all losses), $P_{tot,LT} = (1-0.15)(12)(34) = 347$ kips

Estimated precompression stress (after all losses), $f_{c,tot,LT} = -\frac{P_{tot,LT}}{A_g} = \frac{347}{324} = -1.07$ ksi

Estimated modulus, $E_c = 2500(f_c')^{0.33} = 2500(26.65)^{0.33} = 7{,}386$ ksi

Estimated precompression strain (after all losses), $\varepsilon_{c,tot,LT} = \frac{f_{c,tot,LT}}{E_c} = \frac{1.07}{7{,}386} = -145$ με

Measurements of the top fiber strain taken at three different locations along the pile length near midspan are shown in Figure 30. Figure 30 (a) shows the strain indicated from SG1-3, located one ft. north of the midspan, (b) shows the strain indicated from SG4-6, located at the midspan, (c) shows the strain indicated from SG7-9, located one ft. south of the midspan. At each location, there were three measurement points across the width of the pile. The strain at the maximum load was observed in SG2 as -2,808 με, which is -2,953 με with the inclusion of the estimated precompression strain. Also, the maximum top fiber strain of -3,718 was observed at a load of 71.71 kips in SG2, which is -3,863 με with the inclusion of the estimated precompression strain as shown below:

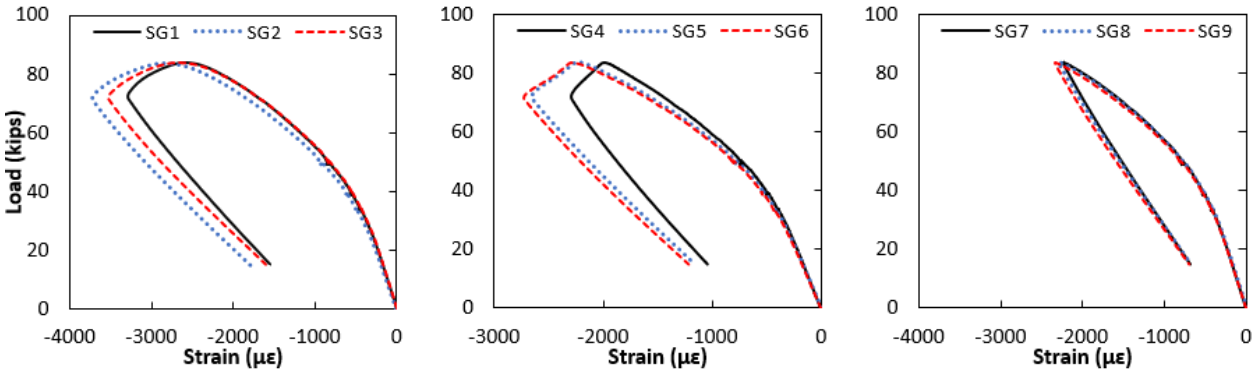

Figure 30: Load versus top fiber (compressive) strain measured for 18-inch square UHPC pile, for gages (a) SG-13, (b) SG4-6, and (c) SG7-9

Compression strain at maximum load, $\varepsilon_{c,83.76\,k} = -2{,}808 - 145 = -2{,}953$ με

Maximum compression strain (at 71.71 kips), $\varepsilon_{c,max} = -3{,}718 - 145 = -3{,}863$ με

In addition to top fiber strain, concrete strain along the depth of the pile section at midspan were recorded at different loads. The strains were measured only for half of the pile depth. Consequently, linear fits of measured values were used to extrapolate strain values across the rest of the pile depth up to the bottom fiber at the different loads as shown in Figure 31. The extrapolated bottom fiber strains are summarized in Table 15, along with the linear correlation and curvature determined from the slope of the measured strain values.

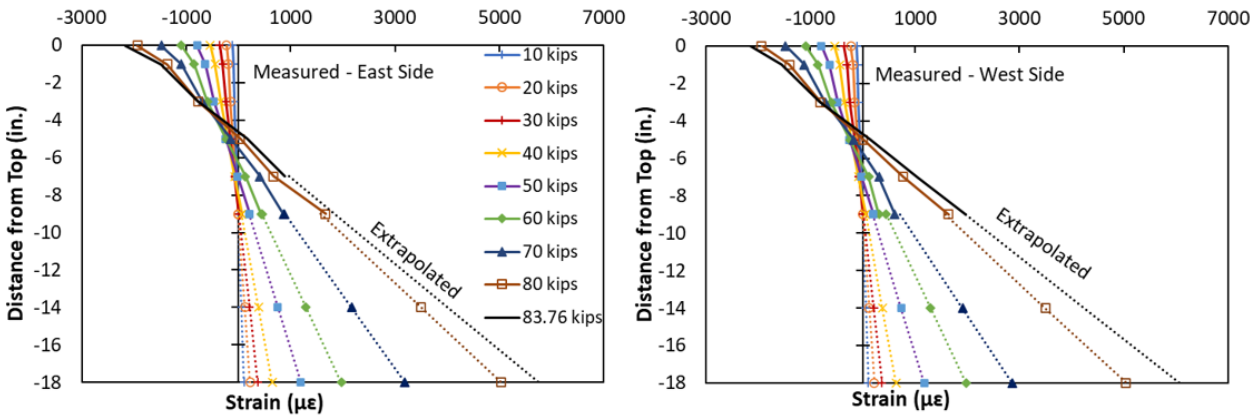

Figure 31: Concrete strain profile along pile depth on (a) the east side and (b) the west side for the 18-inch square UHPC pile at different loads

Table 15: Extrapolated bottom strain, correlation, and curvature for 18-inch square UHPC pile

Load (kips)	East Side			West Side		
	Extrap. Bottom Strain (με)	Correl. (R)	Curv. = Slope^{-1} (1/in.)	Extrap. Bottom Strain (με)	Correl. (R)	Curv. = Slope^{-1} (1/in.)
10	110.2	0.998	1.24E-05	111.9	0.995	1.24E-05
20	223.8	0.998	2.49E-05	224.8	0.996	2.49E-05
30	374.5	0.998	4.05E-05	372.8	0.996	4.03E-05
40	649.2	0.998	6.54E-05	639.5	0.997	6.41E-05
50	1198.0	0.997	1.10E-04	1175.9	0.997	1.09E-04
60	1975.5	0.998	1.69E-04	1802.0	0.993	1.59E-04
70	3194.3	0.997	2.56E-04	2863.4	0.992	2.38E-04
80	5040.5	0.994	3.85E-04	5039.5	0.998	3.85E-04
83.76	5758.0	0.994	4.35E-04	6058.0	0.998	4.55E-04
71.71	6766.6	0.969	5.00E-04	6743.3	0.985	5.00E-04
60	6171	0.964	4.55E-04	6150	0.983	4.55E-04

From the extrapolated bottom fiber (tensile) strains, the tensile strain at the maximum load (including the estimated precompression) was estimated to be 5,913 με as shown below:

Tensile strain at maximum load, $\varepsilon_{t,83.76\,k} = 6{,}058 - 145 = 5{,}913$ με

Maximum tensile strain (at 71.71 kips), $\varepsilon_{t,max} = 6{,}743 - 145 = 6{,}598$ με

Given the assumption that plane sections before bending remain plane after bending, the change in longitudinal compressive or tensile strain profile at midspan is shown in Figure 31. The shift in the neutral axis as the applied load increased is also evident. As shown in Figure 32, strains in gauges SG14 and SG16 transitioned from the compression region at the beginning of the test to the tensile region at the end of the test. The same behavior was also observed with gauges SG15 and SG17 on the west side of the pile. The location of the strain gauges along the depth of the pile section on the east and west sides were summarized in Table 10. Therefore, it can be deduced from the values in the table that the neutral axis shifted from about 9 in. to between 3 in. and 5 in. from the top fiber.

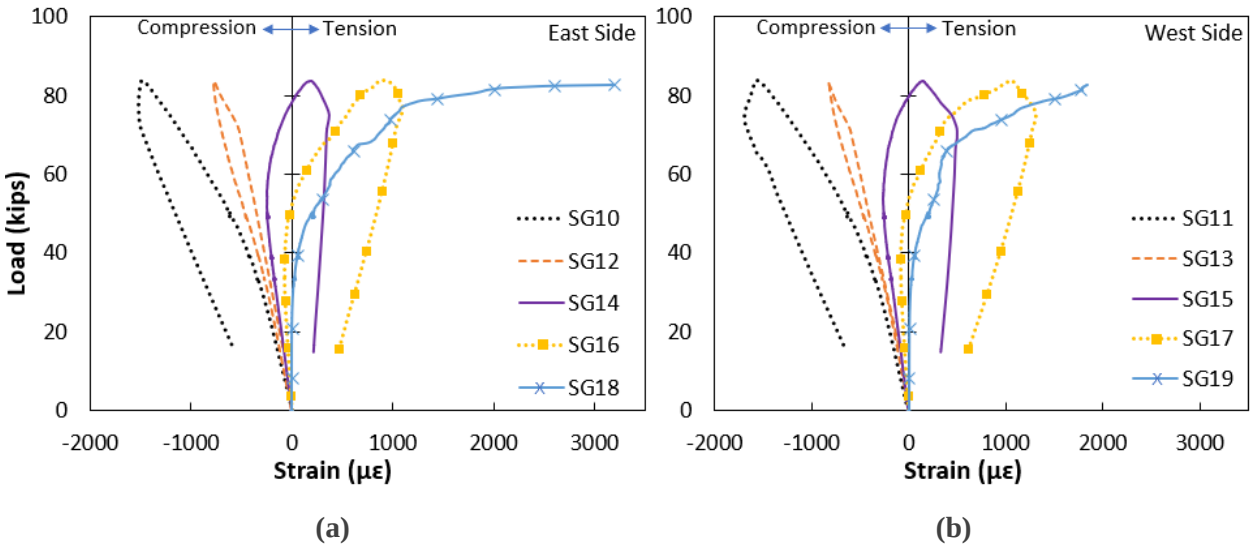

(a) (b)

Figure 32: Change in longitudinal strain on (a) the east side and (b) the west side of the square pile

Also, the moment - curvature response determined from the applied load, estimated self-weight, and measured concrete strains is shown in Figure 33. Based on the measured response, the 18-inch square pile reached its ultimate capacity and then began to lose capacity with strain localization of the UHPC after prestressed strand yielding at 83.76 kips applied load, which is equivalent to maximum moment of 537 k-ft. and a bottom fiber strain of approximately 5,913 με. Also, as shown the maximum curvature (5.00E-04 $in.^{-1}$) occurred at the crushing load.

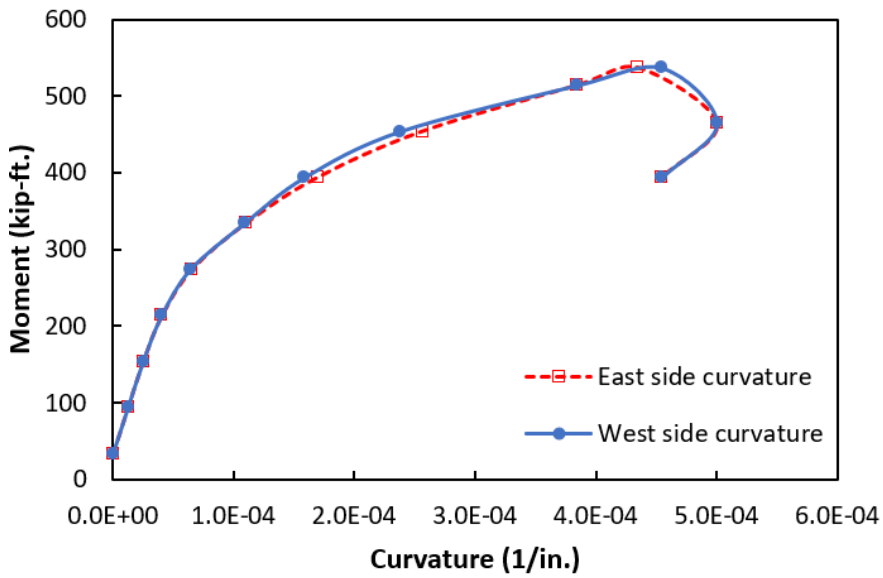

Figure 33: Moment – curvature response of 18-inch square UHPC pile under applied load

Strand slip was assessed at the north and south ends of the pile. The measured response and the summation of strand slip for the bottom strands are as shown in Figure 34. As shown the total slip was between -0.004 in. and +0.002 in, indicative of a good bond between the strands and UHPC.

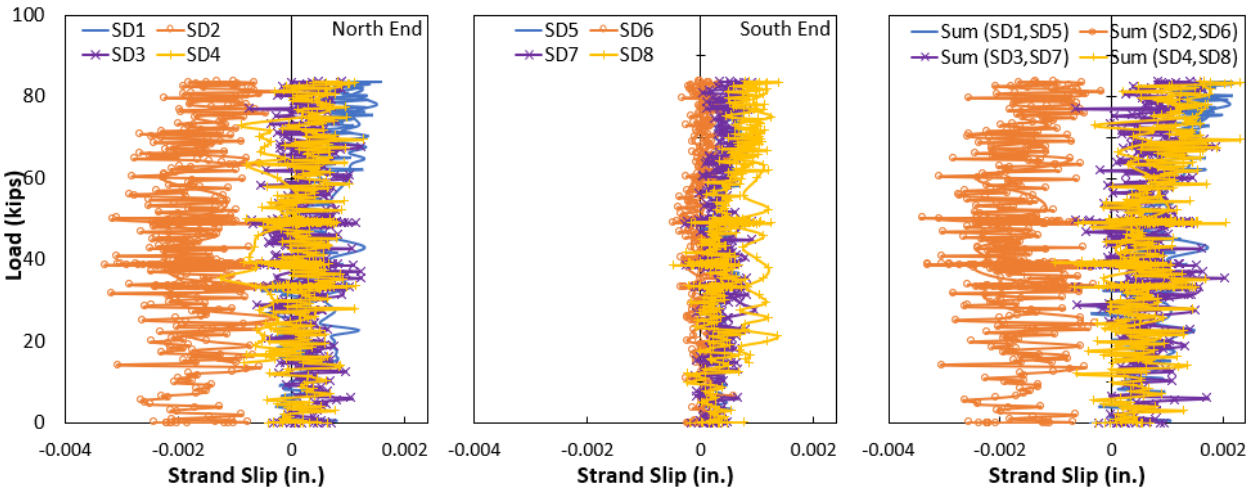

Figure 34: Measured strand slip at the (a) north end (b) south end, and (c) summation of slip at both ends of the 18-inch square UHPC pile

4.1.2 30-inch UHPC H-Pile – Strong Axis

The measured load versus deflection response for the 30-inch UHPC H-Pile tested in flexure about its strong axis is shown in Figure 35. The measured settlement displacements at the supports are subtracted from the other displacement measurements. The average of the two displacement readings taken at three points near midspan are shown in addition to the displacement readings taken at four other points along the pile. The curve appears to be linear up to about 132 kips, which was taken as the cracking load. After prestressed strand yielding occurred, strain localization began at the corner of the bottom flange in the constant moment region and then extended across the width of the bottom flange at a maximum applied load of 249.5 kips and a maximum deflection of 2.18 in. Popping sounds were heard during strain localization as the fibers pulled out. The localization of the crack resulted in an abrupt decrease in load capacity to 202 kips which equates to a 19% decrease, while maximum deflection increased to 2.44 in. After the localization-induced reduction in load capacity, a marginal increase in load capacity to 209 kips was observed with increased deflection to 3.18 in. At 209 kips another abrupt drop in load capacity occurred to 187 kips, which equates to a 10.5% decrease. This was again followed by a marginal increase in load capacity to 190 kips with increased deflection to 3.53 in. Several ruptured strands were observed during specimen testing, this could explain the abrupt drop in load capacity described earlier.

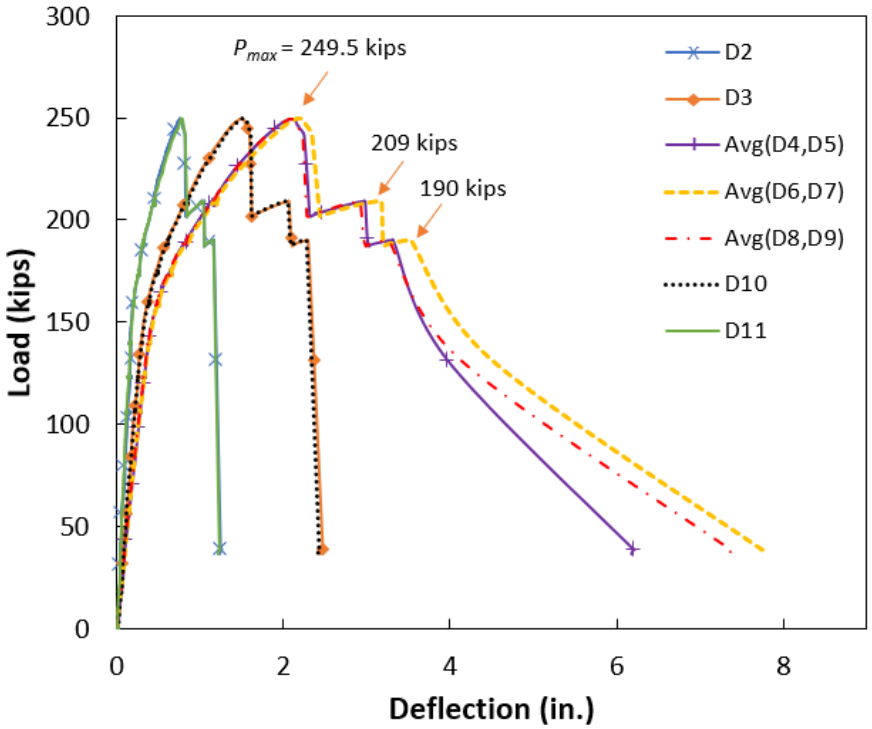

Figure 35: Load versus deflection for 30-inch UHPC H-Pile – strong axis test

Figure 36 shows a plot of deflection along the length of the pile at different applied loads. As shown the pile reached a deflection of 2.18 in. at the ultimate load, however, the pile continued to show strain hardening behavior till complete failure occurred at about 190 kips and a corresponding maximum deflection of 3.53 in.

The moment at the cracking load and maximum load can be found as shown in the following calculations.

Approximate self-weight, $w_{sw} = \rho_c A_g = (0.155\ kcf)(412.5\ in.^2)\left(\frac{1\ ft.}{12\ in.}\right)^2 = 0.444\ {}^{k}/_{ft.}$

Self-weight moment at midspan, $M_{sw,max} = \frac{w_{sw}L^2}{8} = \frac{({}^{0.444k}/_{ft.})(28\ ft.)^2}{8} = 43.5\ k-ft.$

Cracking moment, $M_{cr} = 0.5P_{cr}a + \frac{w_{sw}L^2}{8} = 0.5(132\ kips)(12\ ft.) + 43.5\ k-ft. = 836\ k-ft.$

Maximum moment at failure, $M_{max} = 0.5(249.5\ kips)(12\ ft.) + 43.5\ k-ft. = 1{,}541\ k-ft.$

Precompression strain was determined with the assumptions that there were only axial strains from precompression (because of the symmetrical strand pattern in the pile) and that the total prestress loss was 15 %. The calculations are as follows:

Estimated precompression force (after all losses), $P_{tot,LT} = (1-0.15)(18)(44) = 673.2$ kips

Estimated precompression stress (after all losses), $f_{c,tot,LT} = -\frac{P_{tot,LT}}{A_g} = \frac{673.2}{412.5} = -1.63$ ksi

Estimated modulus, $E_c = 2500(f_c')^{0.33} = 2500(22.76)^{0.33} = 7{,}085$ ksi

Estimated precompression strain (after all losses), $\varepsilon_{c,tot,LT} = \frac{f_{c,tot,LT}}{E_c} = \frac{1.63}{7{,}085} = -230\ \mu\varepsilon$

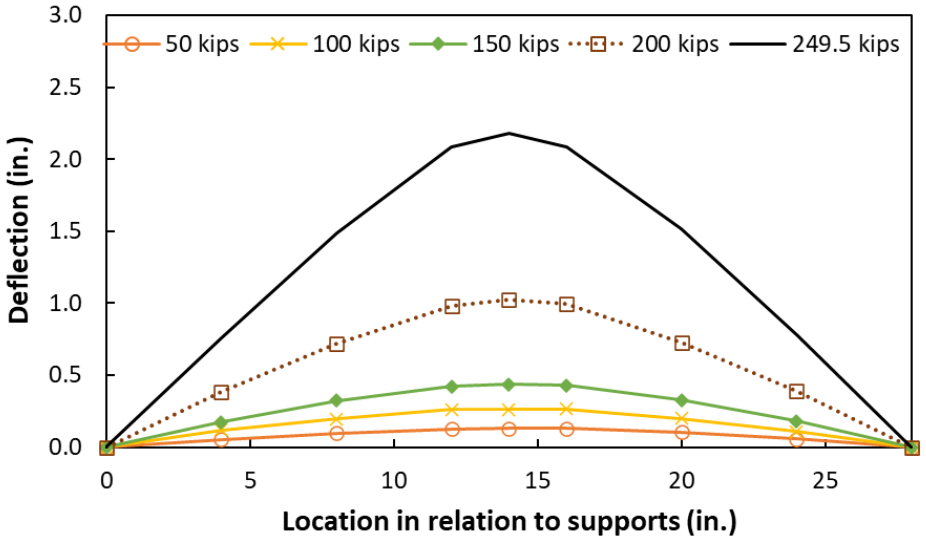

Figure 36: Deflection versus distance from north support for 30-inch UHPC H-Pile – strong axis

Measurements of the top fiber strain taken at three different locations along the pile length near midspan are shown in Figure 37. Figure 37 (a) shows the strain indicated from SG1-3, located one ft. north of the midspan, (b) shows the strain indicated from SG4-6, located at the midspan, (c) shows the strain indicated from SG7-9, located one ft. south of the midspan. At each location, there were three measurement points across the width of the pile. The strain at the maximum load was observed in SG6 as -1,708 με, which is -1,938 με with the inclusion of the estimated precompression strain. At 209 kips, the maximum top fiber strain of -2,875 was observed in SG5, which is -3,105 με with the inclusion of the estimated precompression, while at 190 kips strain was observed in SG5 as -3,144 με, which is -3,374 με with the inclusion of the estimated precompression strain.

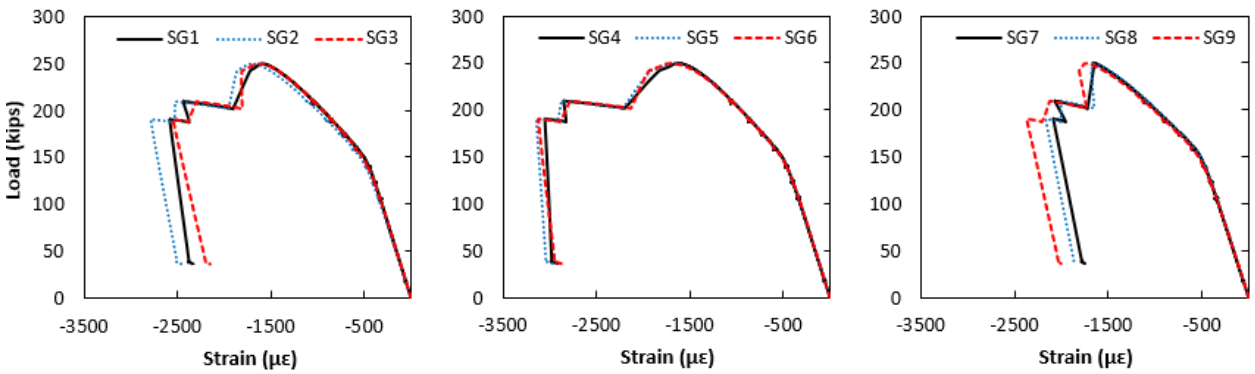

Figure 37: Load versus top fiber (compressive) strain - 30-inch UHPC H-Pile (strong axis test) for gages (a) SG1-3, (b) SG4-6, and (c) SG7-9

In addition to top fiber strain, concrete strain along the depth of the pile section at midspan were recorded at different loads. The location of the strain gauges along the depth of the pile section on the east side only

was summarized in Table 11. Gauges SG10 to SG15 were all installed at the web of the H-Pile. For the uninstrumented portion along the pile depth, linear fits of measured values were used to extrapolate strain values up to the bottom fiber at the different loads as shown in Figure 38. The extrapolated bottom fiber strains are summarized in Table 16, along with the linear correlation and curvature determined from the slope of the measured strain values. Once the maximum load (249.5 kips) was reached, there were not enough functional sensors for a reasonable correlation to be developed beyond the maximum load. From the extrapolated bottom fiber (tensile) strains, the tensile strain at the maximum load (including the estimated precompression) was estimated to be 5,118 με as shown below:

Tensile strain at maximum load, $\varepsilon_{t,249.5\,k} = 5348 - 230 = 5{,}118\ \mu\varepsilon$

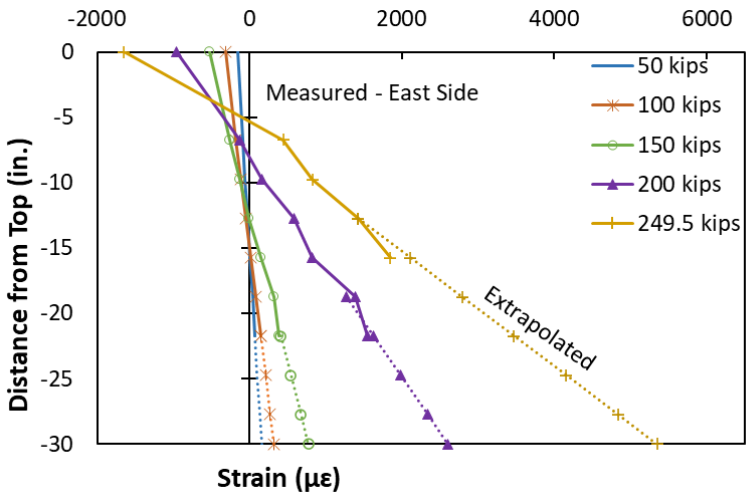

Figure 38: Concrete strain profile along pile depth for the 30-inch UHPC H-Pile (strong axis test) at different loads

Table 16: Extrapolated bottom strain, correlation, and curvature for the 30-inch UHPC H-Pile (strong axis test)

Load (kips)	East Side		
	Extrap. Bottom Strain (με)	Correl. (R)	Curv. = Slope^{-1} (1/in.)
50	159.4	0.999	1.07E-05
100	323.3	0.999	2.16E-05
150	775.5	0.994	4.41E-05
200	2608.8	0.993	1.19E-04
249.5	5348.1	0.967	2.27E-04

Given the assumption that plane sections before bending remain plane after bending, the change in longitudinal compressive or tensile strain profile at midspan is shown in Figure 39. The shift in the neutral axis as the applied load increased can also be observed in Figure 38 and Figure 39. As shown, strains in

gauges SG10, SG11 and SG12 transitioned from the compression region at the beginning of the test to the tensile region at the end of the test. Therefore, it can be deduced from the values in the table that the neutral axis shifted from about 15 in. to less than 6.75 in. from the top fiber.

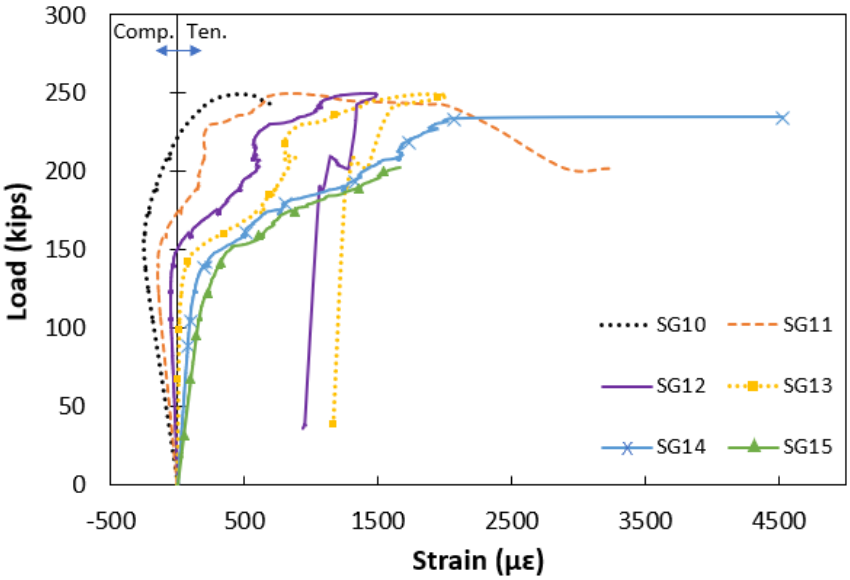

Figure 39: Change in longitudinal strain at the web of the H-Pile on the east side (strong axis test)

The shift in the neutral axis from about 15 in. to less than 6.75 in. from the top fiber is confirmed by the data recorded using the fiber optic sensors. Figure 40 through Figure 44 show the strain recorded by the fiber optic sensors at 50, 100, 150, 200, and 249.5 kips of applied load. The data series title indicates the location of the fiber optic sensor, measured from the top of the UHPC pile. At high loads (200 and 249.5 kips) some of the sensors failed due to cracks or high strain and those sensors are not included in the figures. Figure 44 indicates the neutral axis is less than 6.75 in. from the top fiber. The fiber optic sensors were installed between the two loading points, in the constant moment region of the pile. The data indicates the strain is approximately constant in that region, along the 4 ft length of the fiber sensor. The sensors also confirm that cracking occurred between applied loads of 100 and 150 kips by the sharp strain spike evident in Figure 42.

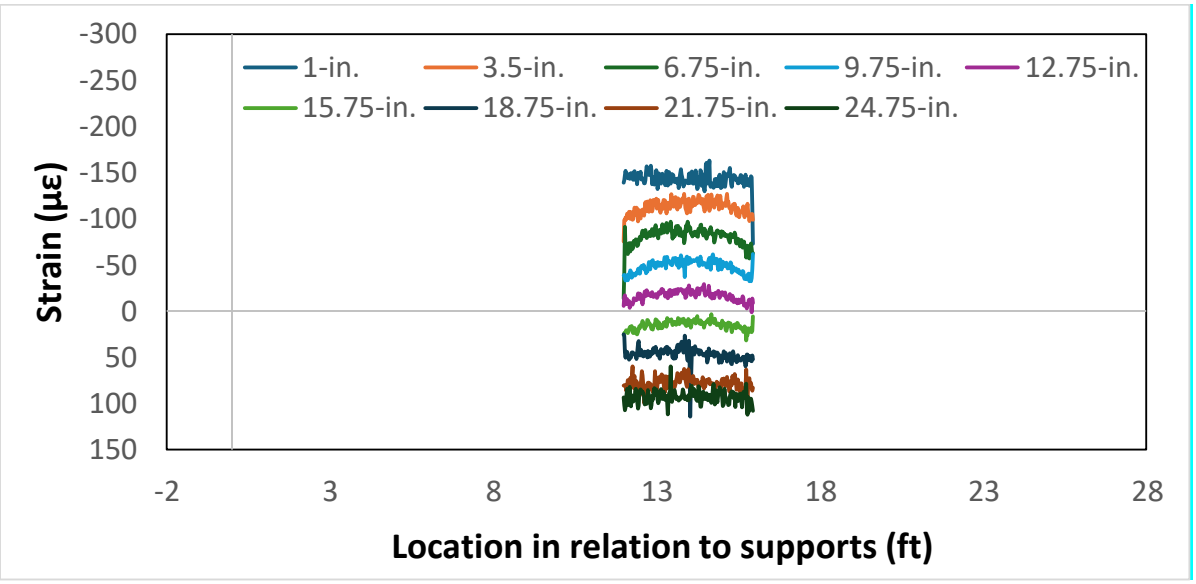

Figure 40: Strain observed in fiber optic sensor at 50 kips

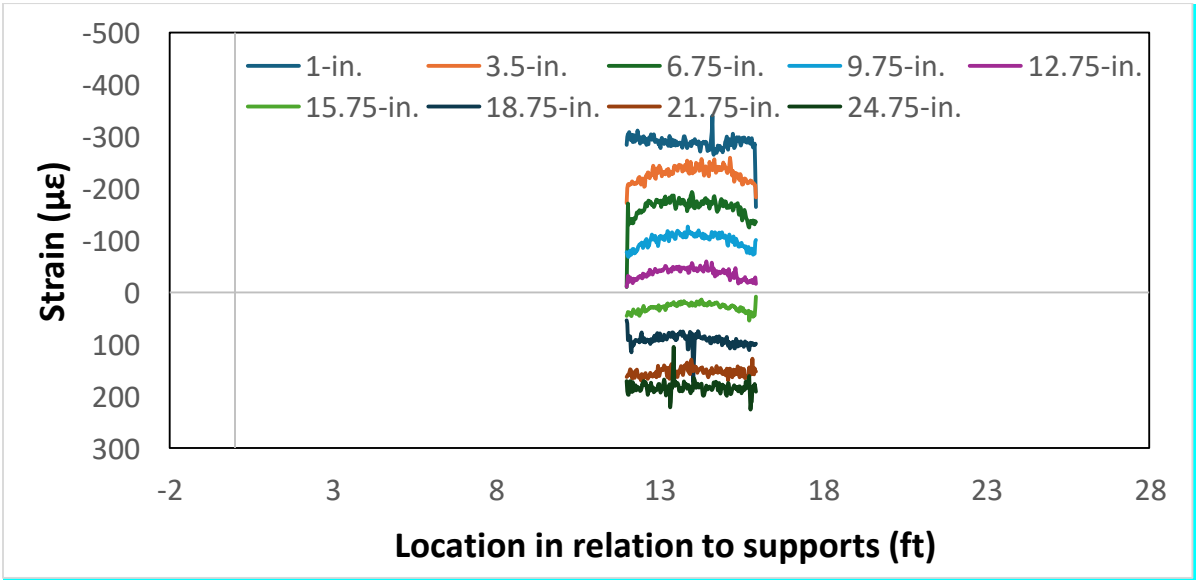

Figure 41: Strain observed in fiber optic sensor at 100 kips

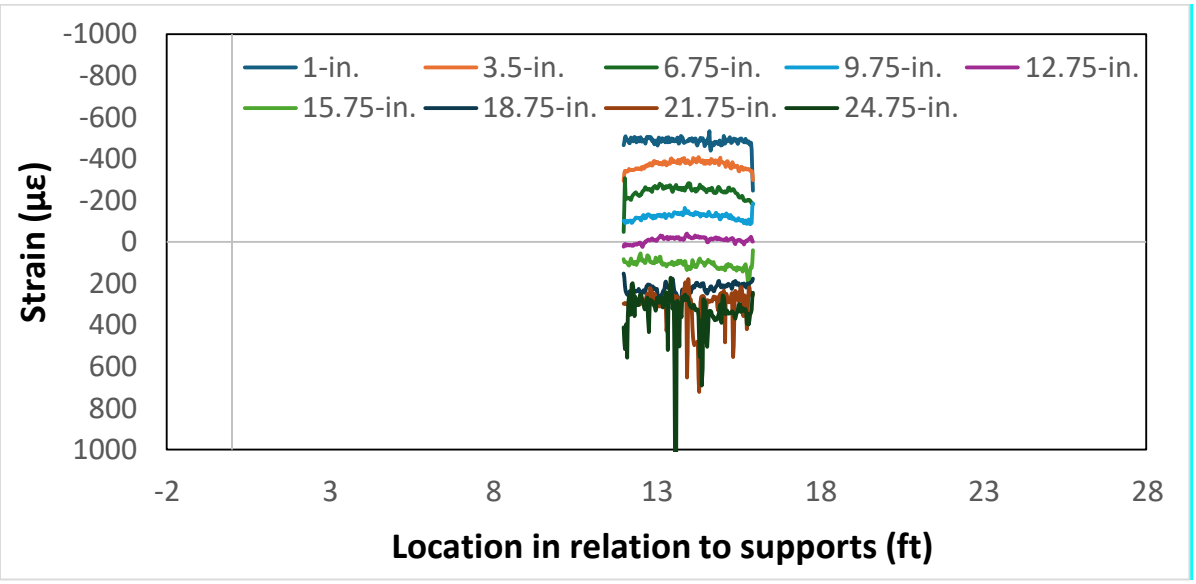

Figure 42: Strain observed in fiber optic sensor at 150 kips

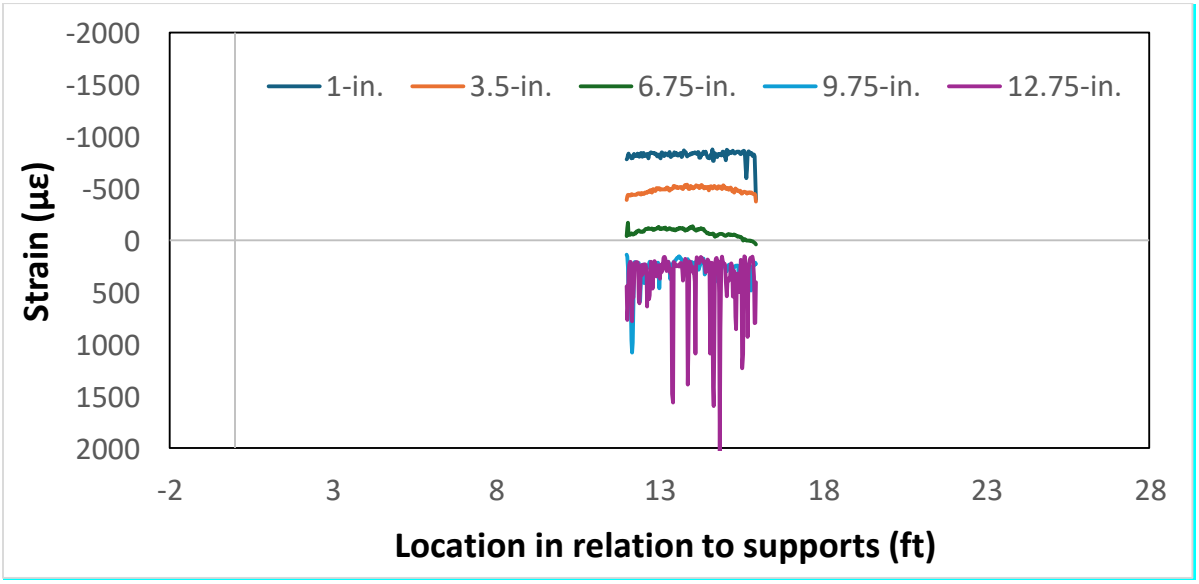

Figure 43: Strain observed in fiber optic sensor at 200 kips

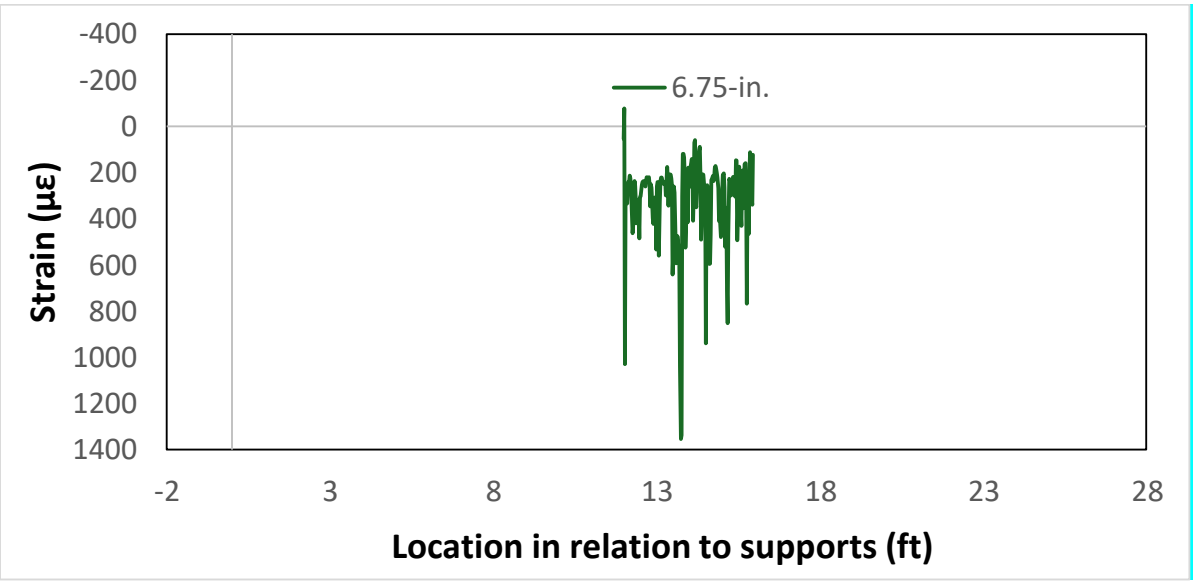

Figure 44: Strain observed in fiber optic sensor at 249.5 kips

The moment - curvature response determined from the applied load, estimated self-weight, and measured concrete strains in Figure 45 shows a maximum moment of 1,541 k-ft. Beyond the maximum moment value, moment – curvature could not be established due to failed gauges.

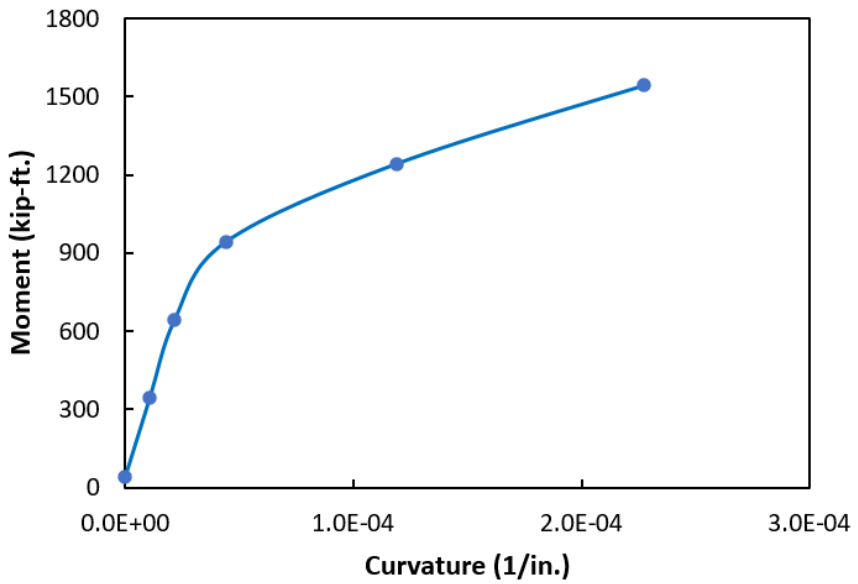

Figure 45: Moment – curvature response of the H-Pile under applied load (strong axis test)

Strand slip was measured at the north and south ends of the pile. The measured response and the summation of strand slip for the bottom strands are as shown in Figure 46. As shown the total slip at maximum load was less than 0.002 in., indicative of a good bond between the strands and UHPC.

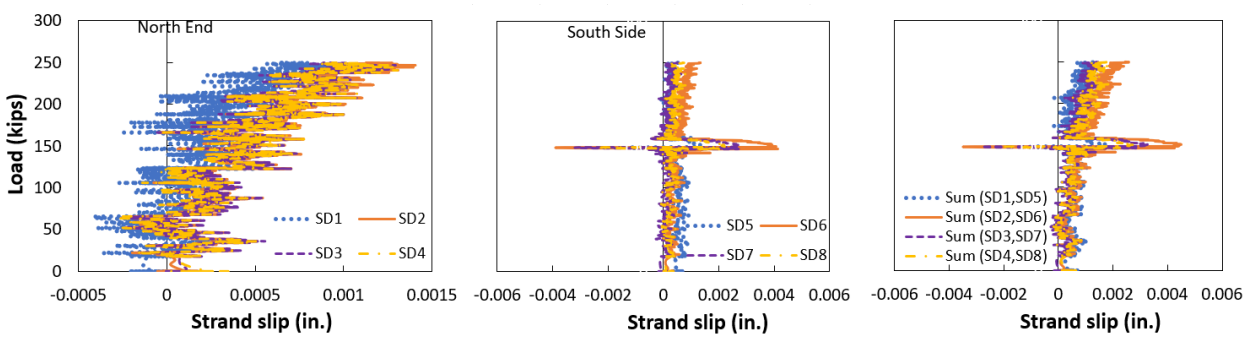

Figure 46: Measured strand slip at the (a) north end (b) south end, and (c) summation of slip at both ends of the 30-inch UHPC H-Pile (strong axis test)

4.1.3 30-inch UHPC H-Pile – Weak axis

The measured load versus displacement response for the 30-inch UHPC H-Pile tested in flexure about its weak axis is shown in Figure 47. The measured displacements at the supports are subtracted from the other displacement measurements. The average of the two displacement readings taken at two points near midspan are shown. The curve appears to go nonlinear around 70 kips, which is assumed to be the cracking load. The maximum applied load and deflection at maximum load was 205.4 kips and 3.83 in., respectively.

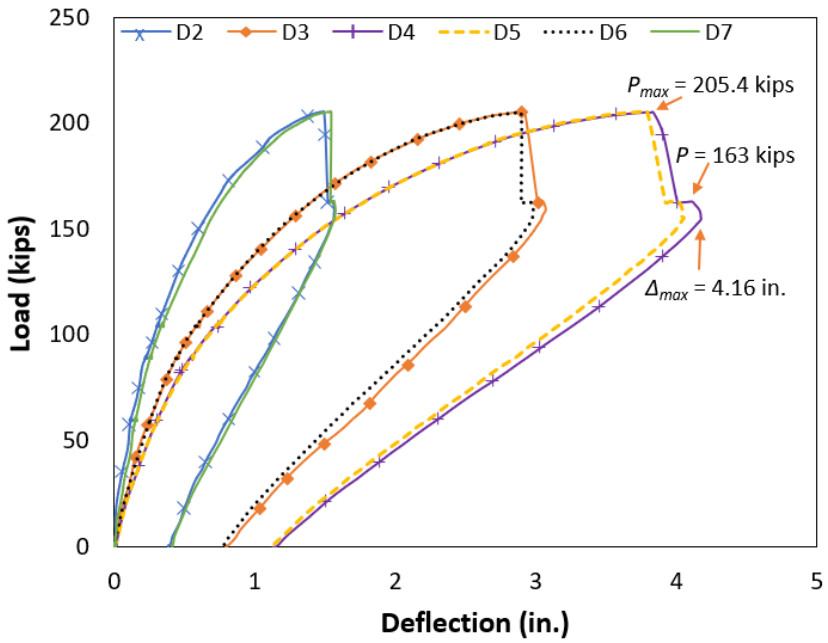

Figure 47: Load versus deflection for 30-inch UHPC H-Pile – weak axis test

At the maximum load, strain localization occurred after prestressed strand yielding with a single large crack opening near midspan. This was accompanied by popping sounds as the fibers at the localization crack pulled out. The localization of the crack resulted in an abrupt decrease in load capacity to 162.5 kips which equates to a 20.9 % decrease, while maximum deflection increased to 4 in. Crushing of the concrete at the top fiber then occurred at 155 kips leading to the failure of the specimen. Figure 48 shows a plot of

deflection along the length of the pile at different applied loads, before strain localization. As shown the pile reached a deflection of 3.83 in. at the ultimate load, however, maximum deflection after strain localization was 4.17 in. at a load of 155 kips.

The moment at the cracking load and maximum load can be found as shown in the following calculations.

Cracking moment, $M_{cr} = 0.5P_{cr}a + \frac{w_{sw}L^2}{8} = 0.5(70\ kips)(12\ ft.) + 43.5\ k-ft. = 463.5\ k-ft.$

Maximum moment at failure, $M_{max} = 0.5(205.4\ kips)(12\ ft.) + 43.5\ k-ft. = 1{,}276\ k-ft.$

Maximum moment at crushing load, $M_{155\ k} = 0.5(155\ kips)(12\ ft.) + 43.5\ k-ft. = 973.5\ k-ft.$

Precompression stress and strain values are -1.63 ksi and -230 με, respectively, as determined for the strong axis test specimen. The values were determined with the assumption that there were only axial strains from precompression due to strand pattern symmetry and that the total prestress loss was 15 %.

The top and bottom fiber strains were measured at midspan on the top and bottom of each flange. Measured values for top and bottom fiber strain are shown in Figure 49. In Figure 49 (a), the maximum compressive strain at the maximum force was observed on the west flange in SG10 as -4,893 με, which is equivalent to -5,123 με when the estimated precompression in the section is included. On the east flange, compressive strain measurements followed the pattern described for the load – deflection curve, and at the crushing load of 155 kips SG1 measured -4,798 με, which is equivalent to -5,028 με with the inclusion of precompression. In Figure 49 (b), the bottom fiber strain gauge SG18 was likely crossing a crack and stopped working at a load of 132 kips.

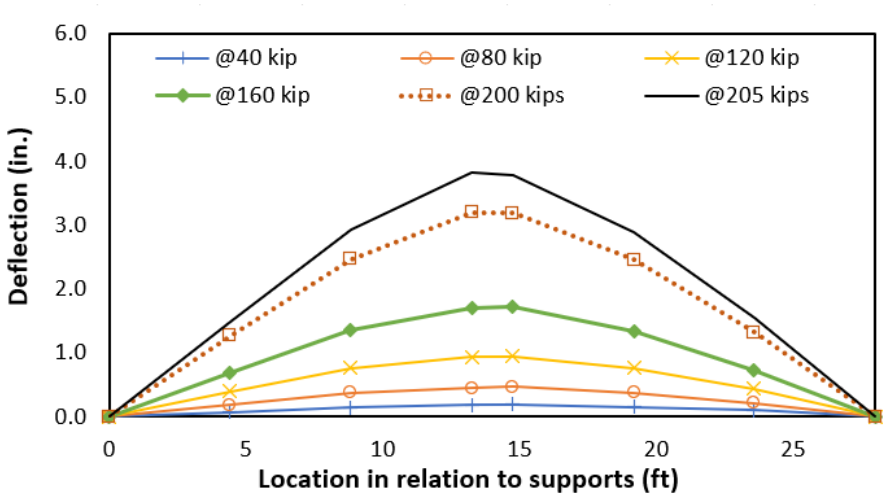

Figure 48: Deflection versus distance from north support for 30-inch UHPC H-Pile – weak axis

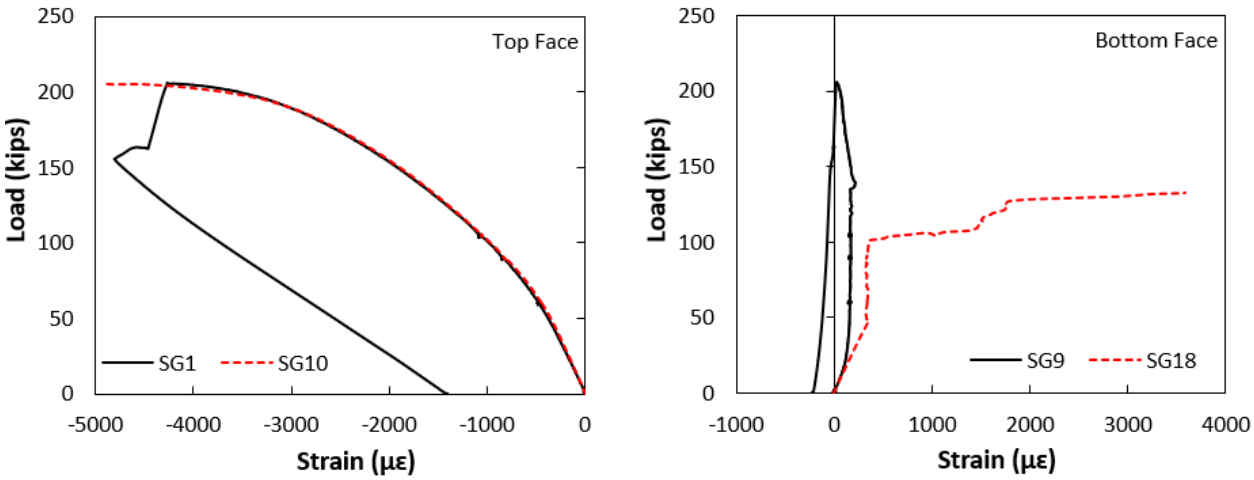

(a) **(b)**

Figure 49: (a) Top fiber strain and (b) bottom fiber strain measured for the H-Pile (weak axis test)

The shift in the neutral axis as the applied load increased can be observed in Figure 50. As shown, strains in gauge SG4 and SG13 on the east and west sides of the pile, respectively, transitioned from the compression region at the beginning of the test to the tensile region at the end of the test. Consequently, it can be deduced from the values in Table 12 that the neutral axis shifted from about 15 in. to between 6 in. and 10 in. from the top fiber.

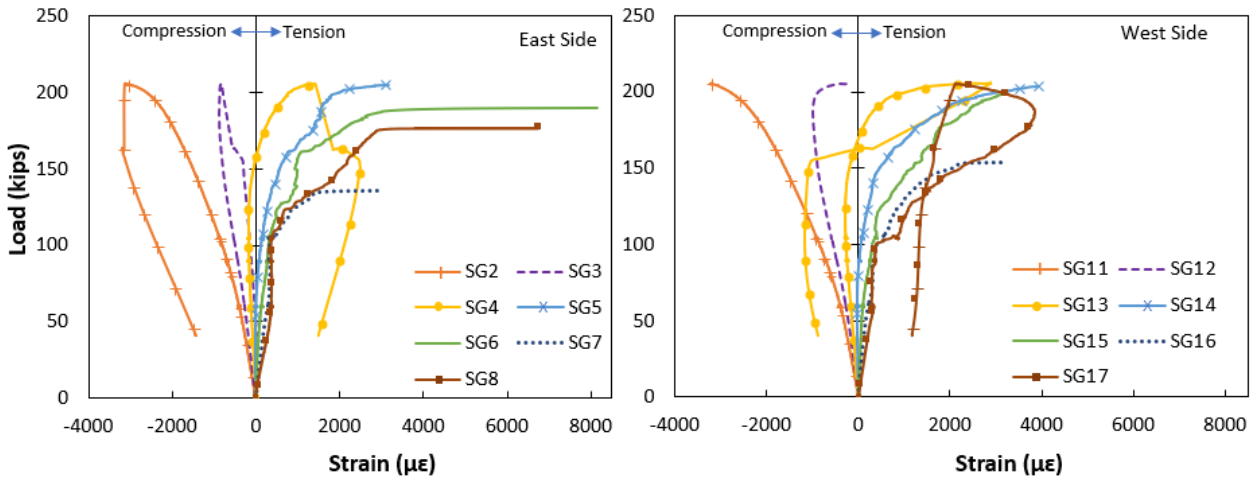

(a) **(b)**

Figure 50: Change in longitudinal strain on the (a) east side and (b) west side of the H-Pile (weak axis test)

The concrete strain across the depth of the section on the east and west faces at midspan at different loads is plotted in Figure 51. The strains were only measured on the flange with some of the gauges not working after a certain load was reached. Therefore, linear extrapolation was used to determine the strains in the faulty gauges at the extreme tension fiber. The extrapolated bottom fiber strains are summarized in Table 17 along with the linear correlation and curvature determined from the slope of the measured strain values. Missing values on this table are due to broken gauges. From the extrapolated bottom fiber (tensile) strains,

the tensile strain at the maximum load (including the estimated precompression) was estimated to be 11,483 με as shown below:

Tensile strain at maximum load, $\varepsilon_{t,205.3\,k} = 11{,}713 - 230 = 11{,}483\ \mu\varepsilon$

Maximum tensile strain at the crushing load (155 kips), $\varepsilon_{t,max} = 16{,}791 - 230 = 16{,}561\ \mu\varepsilon$

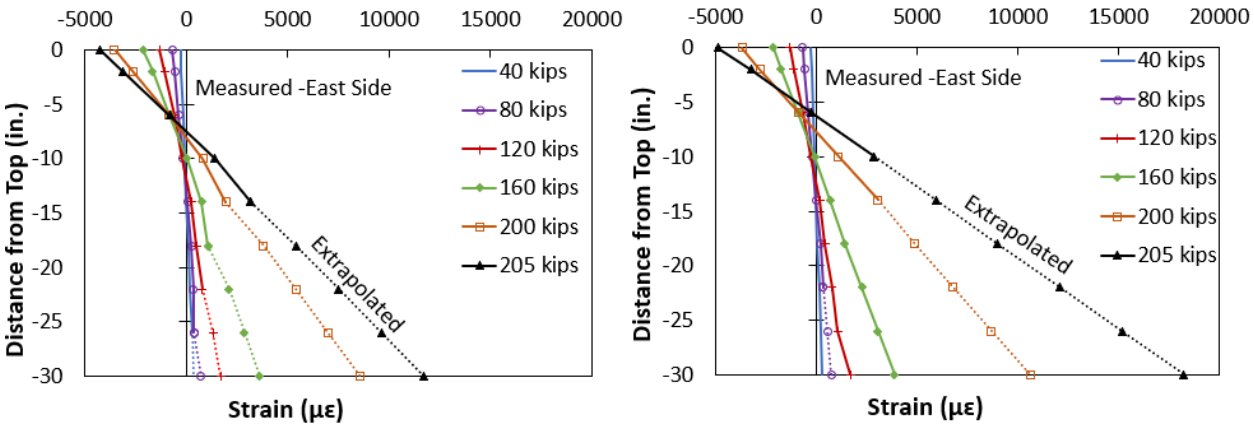

Figure 51: Concrete strain profile along pile depth on (a) the east side and (b) the west side for H-Pile (weak axis test) at different loads

The moment - curvature response of the H-Pile in weak axis flexure is shown in Figure 52. Based on the measured response, the west side measurement showed a much higher curvature (7.69E-04 in.$^{-1}$) at the maximum load compared to the east side curvature measurement (5.26E -04 in.$^{-1}$). This represented a 32 % difference in measured curvature. In addition, the east side curvature was also captured during the loss of capacity beyond the maximum moment. At the crushing moment of 973.5 k-ft., east side curvature peaked at 7.14E-04 in.$^{-1}$.

Table 17: Extrapolated bottom strain, correlation, and curvature for 18-inch square UHPC pile

Load (kips)	East Side			West Side		
	Extrap. Bottom Strain (με)	Correl. (R)	Curv. = Slope^{-1} (1/in.)	Extrap. Bottom Strain (με)	Correl. (R)	Curv. = Slope^{-1} (1/in.)
40	355.1	0.996	2.22E-05	297.1*	0.999	1.92E-05
80	706.2	0.972	4.55E-05	735.5	0.997	4.74E-05
120	1694.5	0.987	9.80E-05	1687.9*	0.993	9.62E-05
160	3619.2	0.981	1.89E-04	3862.5	1.000	2.00E-04
200	8590.9	0.993	4.00E-04	10,603.6	1.000	4.76E-04
205	11713.3	0.997	5.26E-04	18,244.7	1.000	7.69E-04
163	15406.1	1.000	6.67E-04	—	—	—
155	16791.0	0.999	7.14E-04	—	—	—
120	14785.1	0.999	6.25E-04	—	—	—

*Measured value is available so extrapolation is unnecessary.

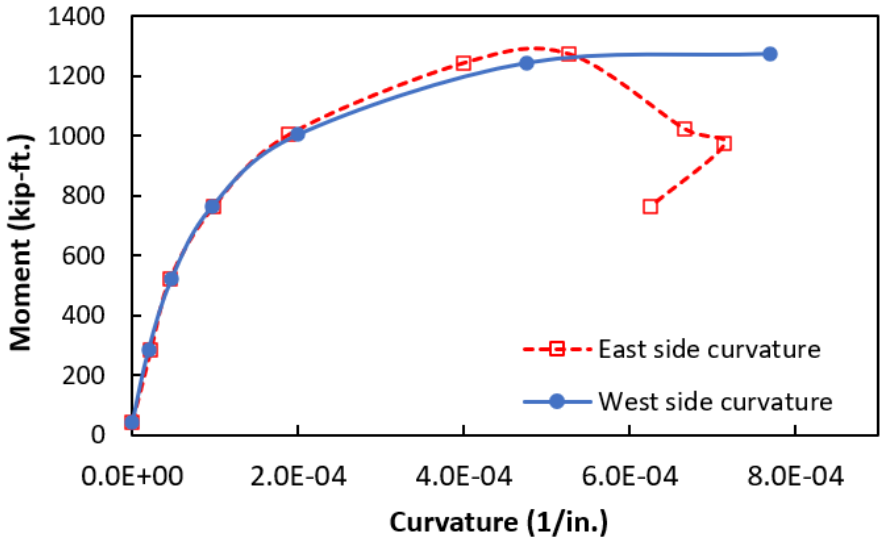

Figure 52: Moment – curvature response of the H-Pile under applied load (weak axis test)

Strand slip was measured at the north and south ends of the pile. The measured response and the summation of strand slip for the bottom strands are as shown in Figure 53. As shown the total slip at maximum load was 0.0015 in., indicative of a good bond between the strands and UHPC.

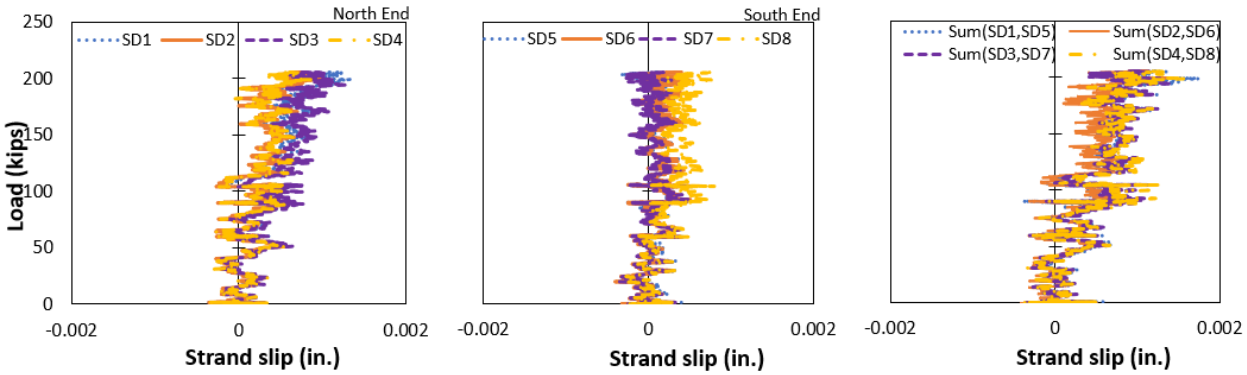

(a) **(b)** **(c)**

Figure 53: Measured strand slip at the (a) north end (b) south end, and (c) summation of slip at both ends of the 30-inch UHPC H-Pile (weak axis test)

4.1.4 24-inch Octagonal UHPC Pile

The measured load versus displacement response for the 24-inch octagonal pile test is shown in Figure 54. The measured displacements at the supports are subtracted from the other displacement measurements. The average of the two displacement readings taken at three points near midspan are shown. The curve appears to go nonlinear around 62 kips, which is taken as the cracking load. The maximum applied load and deflection at maximum load was 133.2 kips and 4.19 in., respectively. At the maximum load, concrete crushing occurred resulting in a sudden loss of load capacity. In addition, Figure 55 shows the progression deflection along the length of the pile at different applied loads.

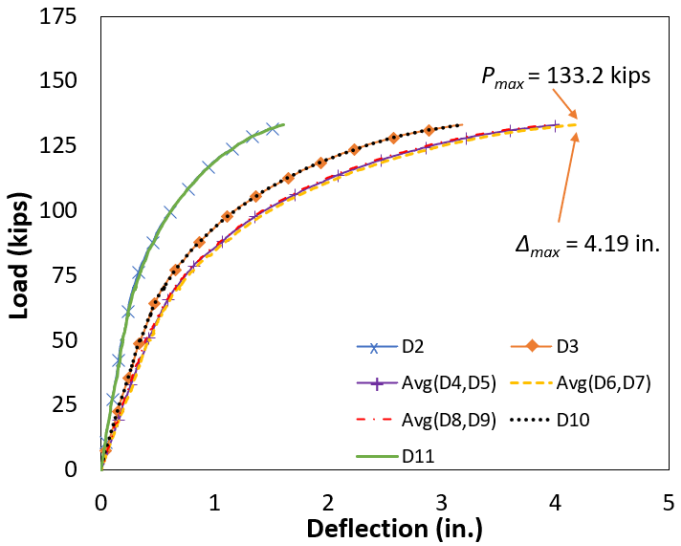

Figure 54: Load versus deflection for the octagonal UHPC pile

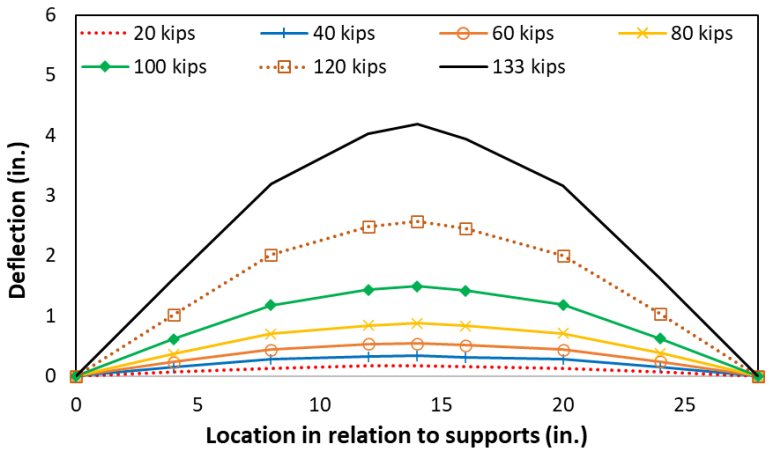

Figure 55: Deflection versus distance from north support for the octagonal UHPC pile

The moment at the cracking load and maximum load can be found as shown in the following calculations.

Approximate area, $A_g = 2\left(1+\sqrt{2}\right)(10\ in.)^2 - \pi(8\ in.)^2 = 281.8\ in.^2$

Approximate self-weight, $w_{sw} = \rho_c A_g = (0.155\ kcf)(281.8\ in.^2)\left(\frac{1\ ft.}{12\ in.}\right)^2 = 0.303\ ^k/_{ft.}$

Self-weight moment at midspan, $M_{sw,max} = \frac{w_{sw}L^2}{8} = \frac{(0.303\ ^k/_{ft.})(28\ ft.)^2}{8} = 29.4\ k-ft.$

Cracking moment, $M_{cr} = 0.5P_{cr}a + \frac{w_{sw}L^2}{8} = 0.5(62\ kips)(12\ ft.) + 29.4\ k-ft. = 401.7\ k-ft.$

Maximum moment at failure, $M_{max} = 0.5(133.2\ kips)(12\ ft.) + 29.4\ k-ft. = 829\ k-ft.$

The strain from the precompression can be estimated as shown below assuming only axial strains from the precompression and a prestress loss of 15 %.

Estimated precompression force (after all losses), $P_{tot,LT} = (1-0.15)(20)(34) = 578$ kips

Estimated precompression stress (after all losses), $f_{c,tot,LT} = -\frac{P_{tot,LT}}{A_g} = \frac{578}{281.8} = -2.05$ ksi

Estimated modulus, $E_c = 2500(f_c')^{0.33} = 2500(19.21)^{0.33} = 6{,}630$ ksi

Estimated precompression strain (after all losses), $\varepsilon_{c,tot,LT} = \frac{f_{c,tot,LT}}{E_c} = \frac{-2.05}{6{,}630} = -309$ με

Measurements of the top fiber strain were taken at three different locations along the pile length near midspan are shown in Figure 56. Figure 56 (a) shows the strain indicated from SG1-3, located one ft. north of the midspan, (b) shows the strain indicated from SG4-6, located at the midspan, (c) shows the strain indicated from SG7-9, located one ft. south of the midspan. At each location, there were three measurement points across the width of the pile. The maximum strain at the maximum force was observed in SG4 as -4,143 με, which is -4,452 με with the inclusion of the estimated precompression strain. When averages were taken as shown in Figure 57, the maximum strain observed was -3,603 με, which is -3,912 με with the inclusion of the estimated precompression strain.

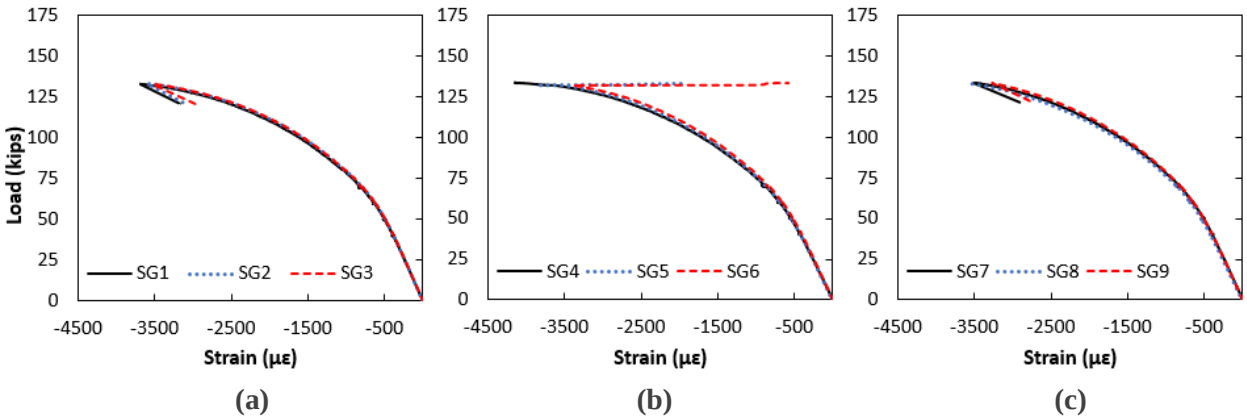

Figure 56: Load versus top fiber (compressive) strain for the octagonal UHPC pile for gages (a) SG1-3, (b) SG4-6, and (c) SG7-9

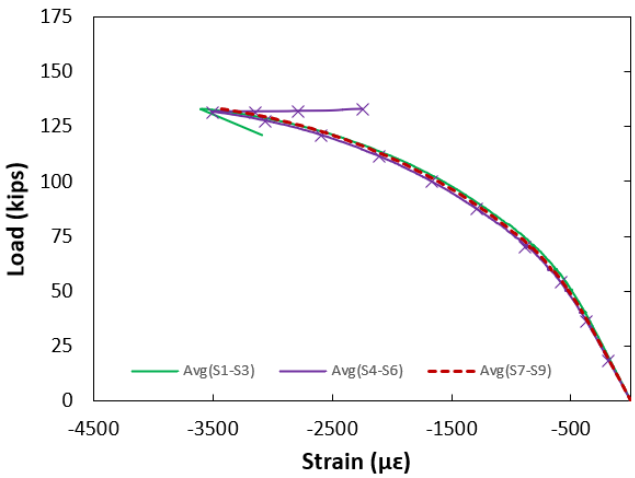

Figure 57: Averaged measurements of the top fiber strain taken at three different locations along the pile length near midspan

No concrete strain gauges were placed on the side faces of the pile, therefore the strain profile along the depth could not be established.

Strand slip was measured at the north and south ends of the pile. The measured response and the summation of strand slip for the bottom strands are as shown in Figure 58. As shown the total slip at maximum load was 0.0013 in., indicative of a good bond between the strands and UHPC.

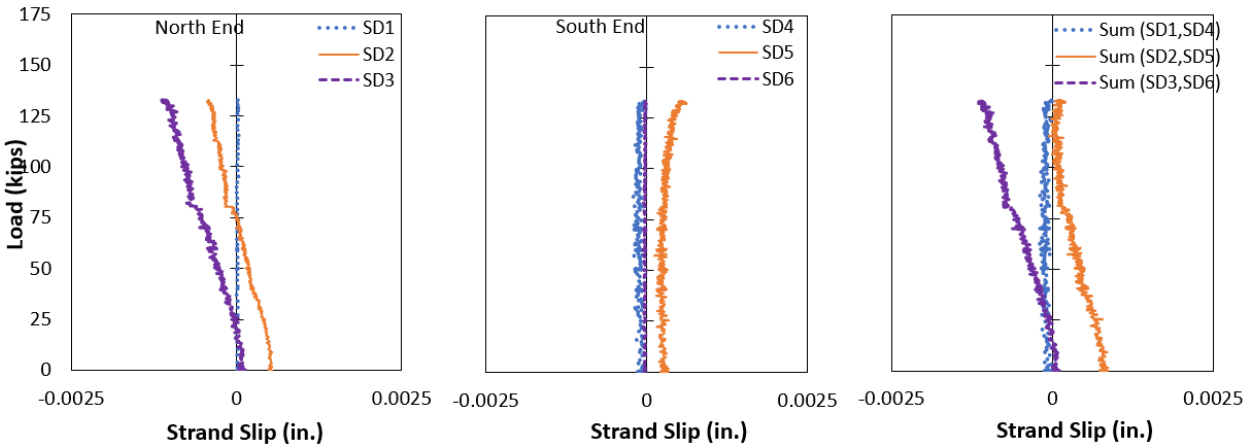

(a) **(b)** **(c)**

Figure 58: Measured strand slip at the (a) north end (b) south end, and (c) summation of slip at both ends of the octagonal UHPC pile

4.2. Failure Mechanism of Specimens

The failure in three of the four specimens, namely 18 in. square pile, H-Pile - strong axis, and H-Pile – weak axis, began with strain localization: the formation of a single larger crack in the constant moment region (see Figure 59 and Figure 60). For all three specimens, strain localization occurred after prestressed strand yielding. Strain localization was accompanied by large popping sounds due to the pulling out of the steel fibers in the UHPC.

The crushing of the concrete in the compression block region occurred after strain localization in the weak axis flexural test of the 30-inch H-Pile, as shown in Figure 60. This crushing of the concrete only occurred on the west top flange of the H-Pile, with the east top flange uncrushed. However, the crack in the bottom of the section extended across the west flange, web, and the east flange as shown in Figure 61.

Concrete crushing in the compression region was also observed for the 24-inch octagonal pile without initial strain localization crack. However, flexural cracks extending throughout the constant moment region were observed in the tension region of the octagonal pile, as shown in Figure 62.

(a) (b)

Figure 59: Strain localization failure in (a) 18-inch square and (b) 30-inch H (strong axis test)

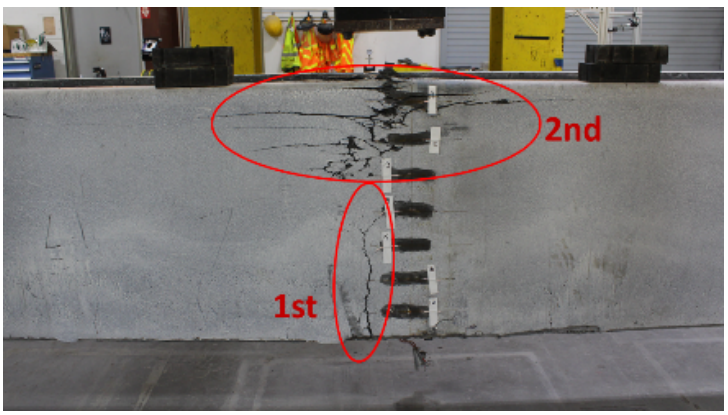

Figure 60: Strain localization failure and concrete crushing in the compression region - 30-inch H (weak axis test)

(a) (b)

Figure 61: Failure of 30-inch H (weak axis test) showing (a) cracked flange from bottom (b) crushed west flange from the top and uncrushed east flange from the top

Figure 62: Failure of the 24-inch octagonal pile

Chapter 5 Discussion

This study investigated the flexural behavior of UHPC piles using four different prestressed specimens, each 30 feet in length. Each pile was statically loaded until failure, in a four-point bending configuration with a 4 ft constant moment region and a 28 ft span. The results from the research conducted provide useful information on the structural integrity and flexural behavior of UHPC.

The specimen with the highest strength of the four was the 30-in. H-Pile (tested in the strong axis orientation). It exhibited a linear response up to approximately 132 kips (836 k-ft) and achieved an ultimate load of 249.5 kips with a deflection of 2.18 inches. After strain localization, the load capacity decreased by 19%. The maximum moment at the time of failure was 1,541 k-ft.

The specimen with the next highest strength was also the H-Pile (tested in the weak axis orientation). The 30-in. H-Pile had a non-linear response at around 70 kips (463.5 k-ft), and a maximum load of 205.4 kips at a deflection of 3.83 inches. Load capacity decreased by 20.9% post strain localization. The maximum moment reached at failure was 1,276 k-ft.

The 24-inch octagonal pile demonstrated non-linear behavior around 62 kips (402 k-ft), with a maximum load of 133.2 kips and a deflection of 4.19 inches. This pile did not show signs of strain localizations but did show signs of concrete crushing and flexural cracks. The maximum moment reached at failure was 829 k-ft.

The specimen with the lowest strength of the tested UHPC piles was the 18-in. square UHPC pile, exhibiting a non-linear response at around 32 kips (226 k-ft), an ultimate load of 83.76 kips and a maximum deflection of 4.56 in. The maximum moment at failure reached 537 k-ft.

Comparing results from the research conducted within this study, the flexural behavior varied with the H-Pile geometry and loading axis. The testing done on the strong axis of the H-Pile showed that the H-Pile proved to be the strongest of the specimens, and the second strongest specimen was also the H-Pile, tested on its weak axis. Following the two H-Piles was the octagonal pile, then the square pile. As previously noted, the geometric configuration of the pile heavily influenced the amount of stress the pile was able to endure.

Looking back to currently available design aids on standard concrete piles, it is clear to see the difference in terms of structural integrity between UHPC and standard concrete. The FDOT Index 455-001 Series Concrete Piles [31] standard plan instructions give analytical data on solid standard concrete piles. Included is a concrete pile with the same size and geometric configuration as the 18in. UHPC square pile discussed within this report. As the tests were conducted in the same manner, we can compare the values from both the standard concrete testing and the UHPC testing. The standard 18-in. concrete square pile has a design maximum moment of approximately 250-290 k-ft, depending on the strand pattern, while the 18-in. UHPC square pile reached a maximum moment of 537 kips-ft. This equates to an approximately 100% average increase in the maximum moment from the standard concrete specimen to the UHPC specimen.

The 24-inch octagonal pile had a 13% smaller cross-sectional area than the 18-in. pile. But with an ultimate strength of 829 k-ft, its capacity exceeded the 18-in. UHPC pile capacity by 50%. The 30 in. UHPC pile had a cross-sectional area that is less than half of the cross-sectional area of a conventional concrete 30 in. pile. However, the capacity is approximately 43% higher in the strong axis orientation and 19% higher in the weak axis orientation. These values are listed in Table 18 below, for further comparison.

Table 18: Area vs. Ultimate Moment Capacity

Concrete Type	Cross Section	Area (in^2)	Ultimate Moment Capacity (k-ft)
Conventional Concrete (f'c = 6500psi)	18" Square	324	Approx. 250-290
	24" Square	576	Approx. 600-650
	30" Square	900	Approx. 1000-1150
Ultra High-Performance Concrete (f'c = 19,212 – 26,645psi)	30" H-Pile (Strong Axis)	412.5	1,541
	30" H-Pile (Weak Axis)		1,276
	24" Octagonal Pile	281.8	829
	18" Square	324.0	537

The flexural behavior of the different UHPC piles varied significantly depending on their geometry and configuration. Both the square and H-Piles exhibited strain localization, which led to significant drops in load capacity post crack formation. The popping sounds heard from the square and H-Piles indicate that the pull-out of the steel fibers in the UHPC contributed to the strain localization. The octagonal pile displayed concrete crushing without initial strain localization, suggesting that the section's geometry and pour influenced its mode of failure and load capacity.

An unexpected result yielded from the testing includes the lack of strain localization in the octagonal pile, contrary to the other specimens. This could be because the method in which the form was secured in such a way that allowed the inner circular void to float when the cement was poured. This could in turn highlight the sensitivity of UHPC performance to geometric imperfections.

Although durability was not the focus of this research, other work has proven that the dense matrix of the UHPC makes it an ideal material for corrosive environments [4] [6] [11]. Knowing the high potential of applications for UHPC within various structures, certain environments with a higher need for durable material can implement UHPC in place of conventional concrete. Currently, the 2024 FDOT Structures Manual [32] states that in extremely aggressive marine environments, piles with carbon or stainless-steel strands, spirals and/or reinforcing are required, along with highly reactive pozzolans for corrosion protection. In marine substructures that hold a pH of less than 5.0, a concentration of Cl greater than 2000ppm, a concentration of SO_4, greater than 1500ppm in water and 2000ppm in soil, or a resistivity less than 500 Ohm-cm, the environment is classified as an extremely aggressive marine environment. As the research conducted within this study highlights the impressive structural integrity and durability of UHPC, UHPC could be used instead of conventional concrete in environments such as extremely aggressive marine environments.

There were a few limitations in the research that are worth noting. One limitation previously noted was the asymmetrical section of the octagonal pile, as it may have influenced the pile's performance and failure mode. Additionally, no strain gauges placed on the side faces of the octagonal pile, which disallowed the collection of data that would complete a strain profile analysis along the depth of the pile.

In a potential follow-up study, it would be necessary to address these limitations to gain a better understanding of UHPC performance. Addressing the geometric imperfections and ensuring symmetrical sections in the pile designs would help in obtaining more reliable and generalizable results. Additionally, the implementation of strain gauges on all faces of the piles would facilitate a comprehensive strain profile analysis, offering more detailed insights into the flexural behavior and failure mechanisms of UHPC. Future studies could also explore a wider range of geometric designs and reinforcement configurations. Analyzing different shapes and sizes of UHPC piles, as well as varying the distribution of internal reinforcement, could provide valuable information on optimizing UHPC performance for specific applications.

The most significant findings from the study highlight UHPC's impressive flexural strength and durability, evidenced by high ultimate loads and substantial deflections before failure. Despite a few limitations in the research conducted, the results collected highlight UHPC's potential for enhancing structural performance in demanding applications. By addressing the limitations mentioned and exploring new avenues in UHPC research, future studies can continue to refine and optimize UHPC applications, ultimately contributing to the development of more efficient durable, and sustainable structural materials. This ongoing research is essential for advancing the field and meeting the evolving needs of infrastructure projects, particularly in regions with more extreme environmental conditions.

The observed deflections and load capacities underscore UHPC's potential for high strength and durability in structural applications. The geometric configurations allow for high strength and durability with less material and overall weight, resulting in lower production and transportation costs, while improving overall durability in structures.

Chapter 6 Conclusions

This study confirms that Ultra-High-Performance Concrete offers a dramatic advancement over conventional concrete in structural applications. The high strength demonstrated by the UHPC specimens, even with geometric variations that can offer reduced overall size and volume when compared with conventional concrete specimens, underscore the material's transformative potential. Evaluating the specimen with the smallest cross-sectional area tested in this study, there is noticeably a large improvement in strength compared to its conventional concrete version. This underscores again how UHPC can be used to meaningfully raise the baseline for structural performance in critical infrastructure.

Based on these conclusions, practitioners should consider UHPC as a viable alternative for marine substructures requiring high durability and corrosion resistance. In extremely aggressive marine environments, UHPC presents an effective solution due to its inherent corrosion resistance and reduced material requirements for similar durability levels.

At the same time, the findings point to a necessary caution: while UHPC possesses superior material properties, its performance is closely tied to the quality and precision of construction. Specimens with internal voids or asymmetric reinforcement are more sensitive to imperfections introduced during fabrication. Subtle geometric or procedural inconsistencies pose consequences, including early strain localization and reduced load carrying capacity. As a result, adopting UHPC at scale will require more than material substitution, it will demand construction practices capable of matching the precision that UHPC performance depends on.

To support widespread adoption, future efforts should focus not only on refining UHPC mix designs and structural geometries, but also on establishing field-ready construction practices that mitigate sensitivity to internal defects and geometric irregularities. Further studies on load performance, long term durability, and the behavior of UHPC under combined environmental and mechanical stress will be essential. Additionally, developing clearer design guidance and quality control protocols will help to pave the way forward to consistent and proper field implementation.

In summary, this study has advanced our understanding of UHPC's flexural behavior, offering practical insights for future applications and laying the groundwork for further investigations into optimizing UHPC performance. The integration of UHPC piles into FDOT projects not only mitigates corrosion concerns but also has the potential to significantly extend the service life of foundation elements, reducing maintenance costs and enhancing the overall resilience of transportation infrastructure. By addressing the identified limitations and exploring new geometric configurations, futures studies can continue to enhance the performance and applicability of UHPC, ultimately contributing to the development of more efficient and durable structural materials.

Bibliography

[1] J. S. Lawler, M. K. Tadros, M. Lampton, E. N. Wagner and A. Sevenker, "Development of Non-Proprietary UHPC for Florida," Iowa State University, Albany, 2019.

[2] K. Wille, A. E. Naaman, S. El-Tawil and G. J. Parra-Montesinos, "Ultra-high performance concrete and fiber reinforced concrete: achieving strength and ductility without heat curing," *Materials and structures*, vol. 45, pp. 309-324, 2012.

[3] P. Y. Blaise and M. Couture, "Precast, Prestressed Pedestrian Bridge—World's First Reactive Powder Concrete Structure," *PCI Journal*, vol. 44, no. 5, p. 60–71, 1999.

[4] B. A. Graybeal and H. G. Russell, "Ultra-High Performance Concrete: A State-of-the-Art Report for the Bridge Community," No. FHWA-HRT-13-060. United States. Federal Highway Administration. Office of Infrastructure Research and Development, McLean, VA, 2013.

[5] B. A. Graybeal, "Ultra-High Performance Concrete," FHWA HRT-11-038 (TechNote), Federal Highway Administration, McLean, VA, 2011.

[6] Z. B. Haber, I. De la Varga, B. A. Graybeal, B. Nakashoji and R. El-Helou, "Properties and Behavior of UHPC-Class Materials," No. FHWA-HRT-18-036. United States. Federal Highway Administration. Office of Infrastructure Research and Development, McLean, VA, 2018.

[7] V. Perry, "The Future of Ultra High-Performance Concrete," *International Interactive Symposium on Ultra-High Performance Concrete*, vol. 3, no. 1, 2023.

[8] A. Arora, Y. Yao, B. Mobasher and N. Neithalath, "Fundamental insights into the compressive and flexural response of binder-and aggregate-optimized ultra-high performance concrete (UHPC).," *Cement and Concrete Composites*, vol. 98, pp. 1-13, 2019.

[9] Z. Li, H. K. Venkata and P. R. Rangaraju, "Influence of silica flour–silica fume combination on the properties of high performance cementitious mixtures at ambient temperature curing," *Construction and Building Materials*, vol. 100, pp. 225-233, 2015.

[10] M. M. Reda, N. G. Shrive and J. E. Gillott, "Microstructural investigation of innovative UHPC," *Cement and Concrete Research*, vol. 29, no. 3, pp. 323-329, 1999.

[11] R. Karim, M. Najimi and B. Shafei, "Assessment of transport properties, volume stability, and frost resistance of non-proprietary ultra-high performance concrete," *Construction and Building Materials*, vol. 227, p. 117031, 2019.

[12] K. Wille and C. Boisvert-Cotulio, "Development of Non-Proprietary Ultra-High Performance Concrete for Use in the Highway Bridge Sector," Federal Highway Administration, McLean, Virginia, 2013, 2013.

[13] W. B. Fuller and S. E. Thompson, "The laws of proportioning concrete," *Transactions of the American Society of Civil Engineers,* vol. 59, no. 2, pp. 67-143, 1907.

[14] A. Andreasen and J. Andersen, "Über die Beziehung zwischen Kornabstufung und Zwischenraum in Produkten aus losen Körnern (mit einigen Experimenten)," *Colloid Polym. Sci.* , vol. 50, no. 3, p. 217–228, 1930.

[15] H. Brouwers and H. Radix, "Self-Compacting Concrete: The Role of The Particle Size," *in the First International Symposium on Design, Performance and Use of Self-Consolidating Concrete (SCC'2005) Changsha, Hunan, China,* pp. 109-118, 2005.

[16] R. Yu, P. Spiesz and H. J. H. Brouwers, "Mix design and properties assessment of ultra-high performance fibre reinforced concrete (UHPFRC)," *Cement and concrete research,* vol. 56, pp. 29-39, 2014.

[17] B. A. Graybeal, "Material Property Characterization of Ultra-High Performance Concrete," (No. FHWA-HRT-06-103). United States. Federal Highway Administration. Office of Infrastructure Research and Development, McLean, VA, 2006.

[18] B. Aarup, "CRC-A Special Fibre Reinforced High Performance Concrete," in *International Symposium on Advances in Concrete through Science and Engineering*, Northwestern, Evanston, Illinois, 2004.

[19] E. M. Williams, S. S. Graham, P. A. Reed and T. S. Rushing, "Laboratory characterization of Cor-Tuf concrete with and without steel fibers," Geotechnical and Structures Laboratory U.S. Army Engineer Research and Development Center, Vicksburg, MS, 2009.

[20] P. Rossi, A. Arca, E. Parant and P. Fakhri, "Bending and compressive behaviours of a new cement composite," *Cement and Concrete Research,* vol. 35, no. 1, pp. 27-33, 2005.

[21] A. S. J. Smith and G. Xu, "Classification of Ultra-high Performance Concrete (UHPC)," *European Journal of Engineering and Technology Research,* vol. 6, no. 6, pp. 87-96, 2021.

[22] R. Vergoossen, "Tailor made bridge design with ultra-high performance concretes," *Tailor Made Concrete Structures,* pp. 1067--1068, 2008.

[23] E. a. D. G. Shahrokhinasab, "Development of "ABC-UTC Non-Proprietary UHPC" Mix," Final Report# ABC-UTC-2016-C2-FIU01-Final, 2021.

[24] T. V. Voort, M. Suleiman and S. Sritharan, "Design and Performance Verification of UHPC Piles for Deep Foundations," Center for Transportation Research and Education Iowa State University, Ames, IA, 2008.

[25] K. Wille, A. E. Naaman and G. J. Parra-Montesinos, "Ultra-High Performance Concrete with Compressive Strength Exceeding 150 MPa (22 ksi): A Simpler Way," *ACI materials journal,* vol. 108, no. 1, 2011.

[26] B. A. Graybeal and F. Baby, "Development of direct tension test method for ultra-high-performance fiber-reinforced concrete," *ACI Materials Journal,* vol. 110, no. 2, p. 177, 2013.

[27] R. G. El-Helou and B. A. Graybeal, "Flexural behavior and design of ultrahigh-performance concrete beams," *Journal of Structural Engineering,* vol. 148, no. 4, p. 04022013, 2022.

[28] M. T. Suleiman, S. Sritharan and T. L. V. Voort, "Ultra-High Performance Concrete in Geotechnical and Substructure Applications," Center for Transportation Research and Education Iowa State University, Ames, IA, 2008.

[29] K. W. Ng, J. Garder and S. Sritharan, "Investigation of ultra high performance concrete piles for integral abutment bridges," *Engineering Structures,* vol. 105, pp. 220--230, 2015.

[30] E. S. T. Villavicencio, "Experimental And Analytical Investigation of UHPC Tensile Strength Behavior," 2021.

[31] Florida Department of Transportation, "Instructions for Design Standards, Index 45-001 Series Concrete Piles," 2025-26. [Online]. Available: https://fdotwww.blob.core.windows.net/sitefinity/docs/default-source/design/standardplans/2026/idx/455-001.pdf?sfvrsn=bc5591d9_1.

[32] Florida Department of Transportation, Structures Manual, Tallahassee: FDOT, 2024.

[33] A. Mirmiran, K. Mackie, M. A. Saleem and J. Xia, "Alternatives to Steel Grid Decks," Florida Department of Transportation, 2009.

[34] A. Mirmiran, K. Mackie, M. A. Saleem, J. Xia, P. Zohrevand and Y. Xiao, "Alternatives to Steel Grid Decks - Phase II," Florida Department of Transportation, 2012.

[35] AASHTO, LRFD Bridge Design Specifications, Seventh Edition, Washington, DC: AASHTO, 2014 with 2015 Interims.

[36] Florida Department of Transportation, FDOT Structures Manual, 2016.

[37] Hardesty & Hanover, LLC, "Bascule Bridge Lightweight Solid Deck Retrofit Research Project Aluminum Orthotropic Deck Research Program Notes," 2015.

[38] URS Corporation, Inc., "Bascule Bridge Lightweight Solid Deck Retrofit Research Project Deck Alternative Screening Report," 2015.

[39] Portland Bolt & Manufacturing Company, Inc., "Bolt Torque Chart," [Online]. Available: http://www.portlandbolt.com/technical/bolt-torque-chart/. [Accessed 11 November 2016].

[40] SC Fastening Systems, LLC, "Torque ASTM A325," [Online]. Available: http://scfastening.com/wp-content/uploads/2015/02/Torque_A325.pdf. [Accessed 11 November 2016].

[41] A. Miranda, A. P. Gerlich and S. Walbridge, "Aluminum Friction Stir Welds: Review of Fatigue Parameter Data and Probabilistic Fracture Mechanics Analysis," *Engineering Fracture Machanics,* vol. 147, no. October 2015, pp. 243-260, 2015.

[42] B. A. Graybeal and B. Stone, "Compression response of a rapid-strengthening ultra-high performance concrete formulation," (No. FHWA-HRT-12-065). United States. Federal Highway Administration. Office of Infrastructure Research and Development., McLean, VA, 2012.

[43] J. Yuan, B. A. Graybeal and K. Zmetra, "Adjacent Box Beam Connections: Performance and Optimization," Federal Highway Administration, McLean, 2018.